

## $B^0 \rightarrow \pi^+ \pi^- \pi^0$ time-dependent Dalitz analysis from Belle

K. Abe,<sup>9</sup> K. Abe,<sup>49</sup> I. Adachi,<sup>9</sup> H. Aihara,<sup>51</sup> D. Anipko,<sup>1</sup> K. Aoki,<sup>25</sup> T. Arakawa,<sup>32</sup>  
 K. Arinstein,<sup>1</sup> Y. Asano,<sup>56</sup> T. Aso,<sup>55</sup> V. Aulchenko,<sup>1</sup> T. Aushev,<sup>21</sup> T. Aziz,<sup>47</sup> S. Bahinipati,<sup>4</sup>  
 A. M. Bakich,<sup>46</sup> V. Balagura,<sup>15</sup> Y. Ban,<sup>37</sup> S. Banerjee,<sup>47</sup> E. Barberio,<sup>24</sup> M. Barbero,<sup>8</sup>  
 A. Bay,<sup>21</sup> I. Bedny,<sup>1</sup> K. Belous,<sup>14</sup> U. Bitenc,<sup>16</sup> I. Bizjak,<sup>16</sup> S. Blyth,<sup>27</sup> A. Bondar,<sup>1</sup>  
 A. Bozek,<sup>30</sup> M. Bračko,<sup>23,16</sup> J. Brodzicka,<sup>9,30</sup> T. E. Browder,<sup>8</sup> M.-C. Chang,<sup>50</sup> P. Chang,<sup>29</sup>  
 Y. Chao,<sup>29</sup> A. Chen,<sup>27</sup> K.-F. Chen,<sup>29</sup> W. T. Chen,<sup>27</sup> B. G. Cheon,<sup>3</sup> R. Chistov,<sup>15</sup>  
 J. H. Choi,<sup>18</sup> S.-K. Choi,<sup>7</sup> Y. Choi,<sup>45</sup> Y. K. Choi,<sup>45</sup> A. Chuvikov,<sup>39</sup> S. Cole,<sup>46</sup> J. Dalseno,<sup>24</sup>  
 M. Danilov,<sup>15</sup> M. Dash,<sup>57</sup> R. Dowd,<sup>24</sup> J. Dragic,<sup>9</sup> A. Drutskoy,<sup>4</sup> S. Eidelman,<sup>1</sup> Y. Enari,<sup>25</sup>  
 D. Epifanov,<sup>1</sup> S. Fratina,<sup>16</sup> H. Fujii,<sup>9</sup> M. Fujikawa,<sup>26</sup> N. Gabyshev,<sup>1</sup> A. Garmash,<sup>39</sup>  
 T. Gershon,<sup>9</sup> A. Go,<sup>27</sup> G. Gokhroo,<sup>47</sup> P. Goldenzweig,<sup>4</sup> B. Golob,<sup>22,16</sup> A. Gorišek,<sup>16</sup>  
 M. Grosse Perdekamp,<sup>11,40</sup> H. Guler,<sup>8</sup> H. Ha,<sup>18</sup> J. Haba,<sup>9</sup> K. Hara,<sup>25</sup> T. Hara,<sup>35</sup>  
 Y. Hasegawa,<sup>44</sup> N. C. Hastings,<sup>51</sup> K. Hayasaka,<sup>25</sup> H. Hayashii,<sup>26</sup> M. Hazumi,<sup>9</sup>  
 D. Heffernan,<sup>35</sup> T. Higuchi,<sup>9</sup> L. Hinz,<sup>21</sup> T. Hokuue,<sup>25</sup> Y. Hoshi,<sup>49</sup> K. Hoshina,<sup>54</sup> S. Hou,<sup>27</sup>  
 W.-S. Hou,<sup>29</sup> Y. B. Hsiung,<sup>29</sup> Y. Igarashi,<sup>9</sup> T. Iijima,<sup>25</sup> K. Ikado,<sup>25</sup> A. Imoto,<sup>26</sup> K. Inami,<sup>25</sup>  
 A. Ishikawa,<sup>51</sup> H. Ishino,<sup>52</sup> K. Itoh,<sup>51</sup> R. Itoh,<sup>9</sup> M. Iwabuchi,<sup>6</sup> M. Iwasaki,<sup>51</sup> Y. Iwasaki,<sup>9</sup>  
 C. Jacoby,<sup>21</sup> M. Jones,<sup>8</sup> H. Kakuno,<sup>51</sup> J. H. Kang,<sup>58</sup> J. S. Kang,<sup>18</sup> P. Kapusta,<sup>30</sup>  
 S. U. Kataoka,<sup>26</sup> N. Katayama,<sup>9</sup> H. Kawai,<sup>2</sup> T. Kawasaki,<sup>32</sup> H. R. Khan,<sup>52</sup> A. Kibayashi,<sup>52</sup>  
 H. Kichimi,<sup>9</sup> N. Kikuchi,<sup>50</sup> H. J. Kim,<sup>20</sup> H. O. Kim,<sup>45</sup> J. H. Kim,<sup>45</sup> S. K. Kim,<sup>43</sup>  
 T. H. Kim,<sup>58</sup> Y. J. Kim,<sup>6</sup> K. Kinoshita,<sup>4</sup> N. Kishimoto,<sup>25</sup> S. Korpar,<sup>23,16</sup> Y. Kozakai,<sup>25</sup>  
 P. Križan,<sup>22,16</sup> P. Krokovny,<sup>9</sup> T. Kubota,<sup>25</sup> R. Kulásík,<sup>4</sup> R. Kumar,<sup>36</sup> C. C. Kuo,<sup>27</sup>  
 E. Kurihara,<sup>2</sup> A. Kusaka,<sup>51</sup> A. Kuzmin,<sup>1</sup> Y.-J. Kwon,<sup>58</sup> J. S. Lange,<sup>5</sup> G. Leder,<sup>13</sup> J. Lee,<sup>43</sup>  
 S. E. Lee,<sup>43</sup> Y.-J. Lee,<sup>29</sup> T. Lesiak,<sup>30</sup> J. Li,<sup>8</sup> A. Limosani,<sup>9</sup> C. Y. Lin,<sup>29</sup> S.-W. Lin,<sup>29</sup>  
 Y. Liu,<sup>6</sup> D. Liventsev,<sup>15</sup> J. MacNaughton,<sup>13</sup> G. Majumder,<sup>47</sup> F. Mandl,<sup>13</sup> D. Marlow,<sup>39</sup>  
 T. Matsumoto,<sup>53</sup> A. Matyja,<sup>30</sup> S. McOnie,<sup>46</sup> T. Medvedeva,<sup>15</sup> Y. Mikami,<sup>50</sup> W. Mitaroff,<sup>13</sup>  
 K. Miyabayashi,<sup>26</sup> H. Miyake,<sup>35</sup> H. Miyata,<sup>32</sup> Y. Miyazaki,<sup>25</sup> R. Mizuk,<sup>15</sup> D. Mohapatra,<sup>57</sup>  
 G. R. Moloney,<sup>24</sup> T. Mori,<sup>52</sup> J. Mueller,<sup>38</sup> A. Murakami,<sup>41</sup> T. Nagamine,<sup>50</sup> Y. Nagasaka,<sup>10</sup>  
 T. Nakagawa,<sup>53</sup> Y. Nakahama,<sup>51</sup> I. Nakamura,<sup>9</sup> E. Nakano,<sup>34</sup> M. Nakao,<sup>9</sup> H. Nakazawa,<sup>9</sup>  
 Z. Natkaniec,<sup>30</sup> K. Neichi,<sup>49</sup> S. Nishida,<sup>9</sup> K. Nishimura,<sup>8</sup> O. Nitoh,<sup>54</sup> S. Noguchi,<sup>26</sup>  
 T. Nozaki,<sup>9</sup> A. Ogawa,<sup>40</sup> S. Ogawa,<sup>48</sup> T. Ohshima,<sup>25</sup> T. Okabe,<sup>25</sup> S. Okuno,<sup>17</sup> S. L. Olsen,<sup>8</sup>  
 S. Ono,<sup>52</sup> W. Ostrowicz,<sup>30</sup> H. Ozaki,<sup>9</sup> P. Pakhlov,<sup>15</sup> G. Pakhlova,<sup>15</sup> H. Palka,<sup>30</sup>  
 C. W. Park,<sup>45</sup> H. Park,<sup>20</sup> K. S. Park,<sup>45</sup> N. Parslow,<sup>46</sup> L. S. Peak,<sup>46</sup> M. Pernicka,<sup>13</sup>  
 R. Pestotnik,<sup>16</sup> M. Peters,<sup>8</sup> L. E. Piilonen,<sup>57</sup> A. Poluektov,<sup>1</sup> F. J. Ronga,<sup>9</sup> N. Root,<sup>1</sup>  
 J. Rorie,<sup>8</sup> M. Rozanska,<sup>30</sup> H. Sahoo,<sup>8</sup> S. Saitoh,<sup>9</sup> Y. Sakai,<sup>9</sup> H. Sakamoto,<sup>19</sup> H. Sakaue,<sup>34</sup>  
 T. R. Sarangi,<sup>6</sup> N. Sato,<sup>25</sup> N. Satoyama,<sup>44</sup> K. Sayeed,<sup>4</sup> T. Schietinger,<sup>21</sup> O. Schneider,<sup>21</sup>  
 P. Schönmeier,<sup>50</sup> J. Schümänn,<sup>28</sup> C. Schwanda,<sup>13</sup> A. J. Schwartz,<sup>4</sup> R. Seidl,<sup>11,40</sup> T. Seki,<sup>53</sup>  
 K. Senyo,<sup>25</sup> M. E. Sevior,<sup>24</sup> M. Shapkin,<sup>14</sup> Y.-T. Shen,<sup>29</sup> H. Shibuya,<sup>48</sup> B. Shwartz,<sup>1</sup>  
 V. Sidorov,<sup>1</sup> J. B. Singh,<sup>36</sup> A. Sokolov,<sup>14</sup> A. Somov,<sup>4</sup> N. Soni,<sup>36</sup> R. Stamen,<sup>9</sup> S. Stanič,<sup>33</sup>  
 M. Starič,<sup>16</sup> H. Stoeck,<sup>46</sup> A. Sugiyama,<sup>41</sup> K. Sumisawa,<sup>9</sup> T. Sumiyoshi,<sup>53</sup> S. Suzuki,<sup>41</sup>  
 S. Y. Suzuki,<sup>9</sup> O. Tajima,<sup>9</sup> N. Takada,<sup>44</sup> F. Takasaki,<sup>9</sup> K. Tamai,<sup>9</sup> N. Tamura,<sup>32</sup>  
 K. Tanabe,<sup>51</sup> M. Tanaka,<sup>9</sup> G. N. Taylor,<sup>24</sup> Y. Teramoto,<sup>34</sup> X. C. Tian,<sup>37</sup> I. Tikhomirov,<sup>15</sup>

K. Trabelsi,<sup>9</sup> Y. T. Tsai,<sup>29</sup> Y. F. Tse,<sup>24</sup> T. Tsuboyama,<sup>9</sup> T. Tsukamoto,<sup>9</sup> K. Uchida,<sup>8</sup>  
Y. Uchida,<sup>6</sup> S. Uehara,<sup>9</sup> T. Uglov,<sup>15</sup> K. Ueno,<sup>29</sup> Y. Unno,<sup>9</sup> S. Uno,<sup>9</sup> P. Urquijo,<sup>24</sup>  
Y. Ushiroda,<sup>9</sup> Y. Usov,<sup>1</sup> G. Varner,<sup>8</sup> K. E. Varvell,<sup>46</sup> S. Villa,<sup>21</sup> C. C. Wang,<sup>29</sup>  
C. H. Wang,<sup>28</sup> M.-Z. Wang,<sup>29</sup> M. Watanabe,<sup>32</sup> Y. Watanabe,<sup>52</sup> J. Wicht,<sup>21</sup> L. Widhalm,<sup>13</sup>  
J. Wiechczynski,<sup>30</sup> E. Won,<sup>18</sup> C.-H. Wu,<sup>29</sup> Q. L. Xie,<sup>12</sup> B. D. Yabsley,<sup>46</sup> A. Yamaguchi,<sup>50</sup>  
H. Yamamoto,<sup>50</sup> S. Yamamoto,<sup>53</sup> Y. Yamashita,<sup>31</sup> M. Yamauchi,<sup>9</sup> Heyoung Yang,<sup>43</sup>  
S. Yoshino,<sup>25</sup> Y. Yuan,<sup>12</sup> Y. Yusa,<sup>57</sup> S. L. Zang,<sup>12</sup> C. C. Zhang,<sup>12</sup> J. Zhang,<sup>9</sup>  
L. M. Zhang,<sup>42</sup> Z. P. Zhang,<sup>42</sup> V. Zhilich,<sup>1</sup> T. Ziegler,<sup>39</sup> A. Zupanc,<sup>16</sup> and D. Zürcher<sup>21</sup>

(The Belle Collaboration)

<sup>1</sup>*Budker Institute of Nuclear Physics, Novosibirsk*

<sup>2</sup>*Chiba University, Chiba*

<sup>3</sup>*Chonnam National University, Kwangju*

<sup>4</sup>*University of Cincinnati, Cincinnati, Ohio 45221*

<sup>5</sup>*University of Frankfurt, Frankfurt*

<sup>6</sup>*The Graduate University for Advanced Studies, Hayama*

<sup>7</sup>*Gyeongsang National University, Chinju*

<sup>8</sup>*University of Hawaii, Honolulu, Hawaii 96822*

<sup>9</sup>*High Energy Accelerator Research Organization (KEK), Tsukuba*

<sup>10</sup>*Hiroshima Institute of Technology, Hiroshima*

<sup>11</sup>*University of Illinois at Urbana-Champaign, Urbana, Illinois 61801*

<sup>12</sup>*Institute of High Energy Physics,*

*Chinese Academy of Sciences, Beijing*

<sup>13</sup>*Institute of High Energy Physics, Vienna*

<sup>14</sup>*Institute of High Energy Physics, Protvino*

<sup>15</sup>*Institute for Theoretical and Experimental Physics, Moscow*

<sup>16</sup>*J. Stefan Institute, Ljubljana*

<sup>17</sup>*Kanagawa University, Yokohama*

<sup>18</sup>*Korea University, Seoul*

<sup>19</sup>*Kyoto University, Kyoto*

<sup>20</sup>*Kyungpook National University, Taegu*

<sup>21</sup>*Swiss Federal Institute of Technology of Lausanne, EPFL, Lausanne*

<sup>22</sup>*University of Ljubljana, Ljubljana*

<sup>23</sup>*University of Maribor, Maribor*

<sup>24</sup>*University of Melbourne, Victoria*

<sup>25</sup>*Nagoya University, Nagoya*

<sup>26</sup>*Nara Women's University, Nara*

<sup>27</sup>*National Central University, Chung-li*

<sup>28</sup>*National United University, Miao Li*

<sup>29</sup>*Department of Physics, National Taiwan University, Taipei*

<sup>30</sup>*H. Niewodniczanski Institute of Nuclear Physics, Krakow*

<sup>31</sup>*Nippon Dental University, Niigata*

<sup>32</sup>*Niigata University, Niigata*

<sup>33</sup>*University of Nova Gorica, Nova Gorica*

<sup>34</sup>*Osaka City University, Osaka*

<sup>35</sup>*Osaka University, Osaka*

<sup>36</sup>*Panjab University, Chandigarh*

<sup>37</sup>*Peking University, Beijing*  
<sup>38</sup>*University of Pittsburgh, Pittsburgh, Pennsylvania 15260*  
<sup>39</sup>*Princeton University, Princeton, New Jersey 08544*  
<sup>40</sup>*RIKEN BNL Research Center, Upton, New York 11973*  
<sup>41</sup>*Saga University, Saga*  
<sup>42</sup>*University of Science and Technology of China, Hefei*  
<sup>43</sup>*Seoul National University, Seoul*  
<sup>44</sup>*Shinshu University, Nagano*  
<sup>45</sup>*Sungkyunkwan University, Suwon*  
<sup>46</sup>*University of Sydney, Sydney NSW*  
<sup>47</sup>*Tata Institute of Fundamental Research, Bombay*  
<sup>48</sup>*Toho University, Funabashi*  
<sup>49</sup>*Tohoku Gakuin University, Tagajo*  
<sup>50</sup>*Tohoku University, Sendai*  
<sup>51</sup>*Department of Physics, University of Tokyo, Tokyo*  
<sup>52</sup>*Tokyo Institute of Technology, Tokyo*  
<sup>53</sup>*Tokyo Metropolitan University, Tokyo*  
<sup>54</sup>*Tokyo University of Agriculture and Technology, Tokyo*  
<sup>55</sup>*Toyama National College of Maritime Technology, Toyama*  
<sup>56</sup>*University of Tsukuba, Tsukuba*  
<sup>57</sup>*Virginia Polytechnic Institute and State University, Blacksburg, Virginia 24061*  
<sup>58</sup>*Yonsei University, Seoul*

## Abstract

We present the results of a time-dependent Dalitz plot analysis of  $B^0 \rightarrow \pi^+ \pi^- \pi^0$  decays based on a  $414\text{fb}^{-1}$  data sample that contains  $449 \times 10^6 B\bar{B}$  pairs collected on the  $\Upsilon(4S)$  resonance with the Belle detector at the KEKB asymmetric energy  $e^+e^-$  collider. The direct  $CP$  violating parameters of  $B^0 \rightarrow \rho^\pm \pi^\mp$  decay mode are measured to be  $\mathcal{A}_{\rho\pi}^{+-} = +0.22 \pm 0.08(\text{stat.}) \pm 0.05(\text{syst.})$  and  $\mathcal{A}_{\rho\pi}^{-+} = +0.08 \pm 0.17(\text{stat.}) \pm 0.12(\text{syst.})$ . We also measure the  $CP$  violating parameters of the decay mode  $B^0 \rightarrow \rho^0 \pi^0$  as  $\mathcal{A}_{\rho^0\pi^0} = -0.45 \pm 0.35(\text{stat.}) \pm 0.32(\text{syst.})$  and  $\mathcal{S}_{\rho^0\pi^0} = +0.15 \pm 0.57(\text{stat.}) \pm 0.43(\text{syst.})$ . Combining our analysis with information on charged  $B$  decay modes, we perform a full Dalitz and isospin analysis and obtain a constraint on the CKM angle  $\phi_2$ ,  $\phi_2 = (83^{+12}_{-23})^\circ$ . A large CKM-disfavored region ( $\phi_2 < 8^\circ$  and  $129^\circ < \phi_2$ ) also remains at 68.3% confidence level.

PACS numbers: 11.30.Er, 12.15.Hh, 13.25.Hw

## 1. INTRODUCTION

In the standard model (SM),  $CP$  violation arises from an irreducible phase in the Cabibbo-Kobayashi-Maskawa (CKM) matrix [1]. The SM predicts that measurement of a  $CP$  asymmetry in time-dependent decay rates of  $B^0$  and  $\bar{B}^0$  gives access to the  $CP$  violating phase in the CKM matrix [2, 3, 4]. The angle  $\phi_2$  of the CKM unitarity triangle can be measured via the tree diagram contribution in  $b \rightarrow u\bar{u}d$  decay processes, such as  $B^0 \rightarrow \pi^+\pi^-$ ,  $B^0 \rightarrow \rho^\pm\pi^\mp$ , or  $B^0 \rightarrow \rho^+\rho^-$  [5]. In these decay processes, however, contributions from so-called penguin diagrams could contaminate the measurement of  $\phi_2$ . Snyder and Quinn pointed out that a Dalitz plot analysis of  $B^0 \rightarrow \rho\pi$ , which includes  $B^0 \rightarrow \rho^+\pi^-$ ,  $B^0 \rightarrow \rho^-\pi^+$ , and  $B^0 \rightarrow \rho^0\pi^0$ , offers a unique way to determine  $\phi_2$  without ambiguity. The Dalitz plot analysis takes into account a possible contamination from a  $b \rightarrow d$  penguin contribution [6]. In addition, an isospin analysis [7, 8] involving the charged decay modes,  $B^+ \rightarrow \rho^+\pi^0$  and  $B^+ \rightarrow \rho^0\pi^+$ , provides further improvement of the  $\phi_2$  determination.

### 1-1. KEKB and Belle Detector

KEKB [9] operates at the  $\Upsilon(4S)$  resonance ( $\sqrt{s} = 10.58$  GeV) with a peak luminosity that exceeds  $1.6 \times 10^{34} \text{ cm}^{-2}\text{s}^{-1}$ .

At KEKB, the  $\Upsilon(4S)$  is produced with a Lorentz boost of  $\beta\gamma = 0.425$  nearly along the electron beamline ( $z$ ). Since the  $B^0$  and  $\bar{B}^0$  mesons are approximately at rest in the  $\Upsilon(4S)$  center-of-mass system (cms),  $\Delta t$  can be determined from the displacement in the  $z$  direction,  $\Delta z$ , between the vertices of the two  $B$  mesons:  $\Delta t \simeq \Delta z/\beta\gamma c$ .

The Belle detector is a large-solid-angle magnetic spectrometer that consists of a silicon vertex detector (SVD), a 50-layer central drift chamber (CDC), an array of aerogel threshold Čerenkov counters (ACC), a barrel-like arrangement of time-of-flight scintillation counters (TOF), and an electromagnetic calorimeter comprised of CsI(Tl) crystals (ECL) located inside a super-conducting solenoid coil that provides a 1.5 T magnetic field. An iron flux-return located outside of the coil is instrumented to detect  $K_L^0$  mesons and to identify muons (KLM). The detector is described in detail elsewhere [10]. Two inner detector configurations were used. A 2.0 cm beampipe and a 3-layer silicon vertex detector was used for the first data sample of  $152 \times 10^6 B\bar{B}$  pairs (DS-I), while a 1.5 cm beampipe, a 4-layer silicon detector and a small-cell inner drift chamber were used to record the remaining  $297 \times 10^6 B\bar{B}$  pairs (DS-II) [11].

### 1-2. Analysis flow

The analysis proceeds in the following steps. First, we extract the signal fraction (Sec. 2). We then determine the sizes and phases of the contributions from radial excitations (Sec. 3). Using the parameters determined in the steps above, we perform a time-dependent Dalitz plot analysis (Sec. 4-6). The fit results are interpreted as quasi-two-body  $CP$  violation parameters (Sec. 7) and are used to constrain the CKM angle  $\phi_2$  (Sec. 8).

### 1-3. Differential decay width of time-dependent Dalitz plot

We measure the decay process  $B^0 \rightarrow \pi^+ \pi^- \pi^0$ , where we denote the four-momenta of the  $\pi^+$ ,  $\pi^-$ , and  $\pi^0$  by  $p_+$ ,  $p_-$ , and  $p_0$ , respectively. The invariant-mass squared of their combinations

$$s_+ = (p_+ + p_0)^2, \quad s_- = (p_- + p_0)^2, \quad s_0 = (p_+ + p_-)^2 \quad (1)$$

satisfies the following equation

$$s_+ + s_- + s_0 = m_{B^0}^2 + 2m_{\pi^+}^2 + m_{\pi^0}^2 \quad (2)$$

by energy and momentum conservation. The differential (time-integrated) decay width with respect to the variables above (Dalitz plot) is

$$d\Gamma = \frac{1}{(2\pi)^3} \frac{|A_{3\pi}^{(-)}|^2}{8m_{B^0}^2} ds_+ ds_- , \quad (3)$$

where  $A_{3\pi}^{(-)}$  is the Lorentz-invariant amplitude of the  $B^0(\overline{B}^0) \rightarrow \pi^+ \pi^- \pi^0$  decay.

In the decay chain  $\Upsilon(4S) \rightarrow B^0 \overline{B}^0 \rightarrow f_1 f_2$ , where one of the  $B$ 's decays into final state  $f_1$  at time  $t_1$  and the other decays into another final state  $f_2$  at time  $t_2$ , the time dependent amplitude is

$$A(t_1, t_2) \sim e^{-(\Gamma/2+iM)(t_1+t_2)} \left\{ \cos[\Delta m_d(t_1 - t_2)/2] (A_1 \overline{A}_2 - \overline{A}_1 A_2) - i \sin[\Delta m_d(t_1 - t_2)/2] \left( \frac{p}{q} A_1 A_2 - \frac{q}{p} \overline{A}_1 \overline{A}_2 \right) \right\} . \quad (4)$$

Here,  $p$  and  $q$  define the mass eigenstates of neutral  $B$  mesons as  $pB^0 \pm q\overline{B}^0$ , with average mass  $M$  and width  $\Gamma$ , and mass difference  $\Delta m_d$ . The width difference is assumed to be zero.

The decay amplitudes are defined as follows,

$$A_1 \equiv A(B^0 \rightarrow f_1) , \quad (5)$$

$$\overline{A}_1 \equiv A(\overline{B}^0 \rightarrow f_1) , \quad (6)$$

$$A_2 \equiv A(B^0 \rightarrow f_2) , \quad (7)$$

$$\overline{A}_2 \equiv A(\overline{B}^0 \rightarrow f_2) . \quad (8)$$

In this analysis, we take  $A_{3\pi}$  as  $A_1$  and choose  $f_2$  to be a flavor eigenstate, i.e.,  $A_2 = 0$  or  $\overline{A}_2 = 0$ . Here we call the  $B$  decaying into  $f_1 = f_{CP} = \pi^+ \pi^- \pi^0$  the  $CP$  side  $B$  while the other  $B$  is the tag side  $B$ ,  $f_2 = f_{tag}(\overline{f}_{tag})$ . The differential decay width dependence on time difference  $\Delta t \equiv t_{CP} - t_{tag}$  is then,

$$d\Gamma \sim e^{-\Gamma|\Delta t|} \left\{ (|A_{3\pi}|^2 + |\overline{A}_{3\pi}|^2) - q_{tag} \cdot (|A_{3\pi}|^2 - |\overline{A}_{3\pi}|^2) \cos(\Delta m_d \Delta t) + q_{tag} \cdot 2\text{Im} \left[ \frac{q}{p} A_{3\pi}^* \overline{A}_{3\pi} \right] \sin(\Delta m_d \Delta t) \right\} d\Delta t , \quad (9)$$

where we assume  $|q/p| = 1$  ( $CP$  and  $CPT$  conservation in the mixing) and  $|A(B^0 \rightarrow f_{\text{tag}})| = |A(\bar{B}^0 \rightarrow \bar{f}_{\text{tag}})|$ , and integrate over  $t_{\text{sum}} = t_{CP} + t_{\text{tag}}$ . Here  $q_{\text{tag}}$  is the  $b$ -flavor charge and  $q_{\text{tag}} = +1(-1)$  when the tag side  $B$  decays into a  $B^0$  ( $\bar{B}^0$ ) flavor eigenstate.

Combining the Dalitz plot decay width (3) and the time dependent decay width (9), we obtain the time dependent Dalitz plot decay width

$$d\Gamma \sim |A(\Delta t; s_+, s_-)|^2 d\Delta t ds_+ ds_- , \quad (10)$$

where

$$|A(\Delta t; s_+, s_-)|^2 = e^{-\Gamma|\Delta t|} \left\{ (|A_{3\pi}|^2 + |\bar{A}_{3\pi}|^2) \right. \\ \left. - q_{\text{tag}} \cdot (|A_{3\pi}|^2 - |\bar{A}_{3\pi}|^2) \cos(\Delta m_d \Delta t) + q_{\text{tag}} \cdot 2\text{Im} \left[ \frac{q}{p} A_{3\pi}^* \bar{A}_{3\pi} \right] \sin(\Delta m_d \Delta t) \right\} , \quad (11)$$

$$A_{3\pi} = A_{3\pi}(s_+, s_-) , \quad \bar{A}_{3\pi} = \bar{A}_{3\pi}(s_+, s_-) . \quad (12)$$

Although there could exist contributions from  $B^0$  decays into non- $\rho\pi$   $\pi^+\pi^-\pi^0$  final states, such as  $f_0(980)\pi^0$ ,  $f_0(600)\pi^0$ ,  $\omega\pi^0$ , and non-resonant  $\pi^+\pi^-\pi^0$ , we confirm that these contributions are small and their effects are taken into account as systematic uncertainties (Sec. 6.6-5). We therefore assume that the  $B^0 \rightarrow \pi^+\pi^-\pi^0$  decay is dominated by the  $B^0 \rightarrow (\rho\pi)^0$  amplitudes:  $B^0 \rightarrow \rho^+\pi^-$ ,  $B^0 \rightarrow \rho^-\pi^+$ , and  $B^0 \rightarrow \rho^0\pi^0$ , where  $\rho$  can be  $\rho(770)$ ,  $\rho(1450)$ , or  $\rho(1700)$ . The Dalitz plot amplitude  $A_{3\pi}(s_+, s_-)$  can then be written as

$$A_{3\pi}(s_+, s_-) = f_+(s_+, s_-)A^+ + f_-(s_+, s_-)A^- + f_0(s_+, s_-)A^0 , \quad (13)$$

$$\frac{q}{p} \bar{A}_{3\pi}(s_+, s_-) = \bar{f}_+(s_+, s_-)\bar{A}^+ + \bar{f}_-(s_+, s_-)\bar{A}^- + \bar{f}_0(s_+, s_-)\bar{A}^0 , \quad (14)$$

where the functions  $f_\kappa(s_+, s_-)$  (with  $\rho$  charge  $\kappa = +, -, 0$ ) incorporate the kinematic and dynamical properties of the  $B^0$  decay into a vector  $\rho$  and a pseudoscalar  $\pi$ . The goal of this analysis is to measure the complex coefficients  $A^+$ ,  $A^-$ ,  $A^0$ ,  $\bar{A}^+$ ,  $\bar{A}^-$ , and  $\bar{A}^0$ ; and constrain the CKM angle  $\phi_2$  using them.

#### 1-4. Kinematics of $B^0 \rightarrow (\rho\pi)^0$

The function  $f_\kappa(s_+, s_-)$  can be factorized into two parts as

$$f_\kappa^{(-)}(s_+, s_-) = T_J^\kappa F_\pi(s_\kappa) \quad (\kappa = +, -, 0) , \quad (15)$$

where  $F_\pi(s_\kappa)$  and  $T_J^\kappa$  correspond to the lineshape of  $\rho$  and the helicity distribution of the  $\rho$ , respectively. Here we assume that a single unique functional form for the lineshape  $F_\pi(s)$  can be used for all six  $(\bar{f}_\kappa)$  [27]. Since this assumption has no good theoretical or experimental foundation, we check the goodness of the assumption with data and assign systematic errors.

The lineshape is parameterized with Breit-Wigner functions corresponding to the  $\rho(770)$ ,  $\rho(1450)$ , and  $\rho(1700)$  resonances:

$$F_\pi(s) = BW_{\rho(770)} + \beta \cdot BW_{\rho(1450)} + \gamma \cdot BW_{\rho(1700)} , \quad (16)$$

where the amplitudes  $\beta$  and  $\gamma$  (denoting the relative size of two resonances) are complex numbers. We use the Gounaris-Sakurai(GS) model [12] for the Breit-Wigner shape.

In the case of pseudoscalar-vector ( $J = 1$ ) decay,  $T_J^\kappa$  is given by

$$T_1^\kappa = -4|\vec{p}_j||\vec{p}_k| \cos \theta^{jk} , \quad (17)$$

$$\begin{cases} T_1^+ = -4|\vec{p}_+||\vec{p}_-| \cos \theta^{+-} , \\ T_1^- = -4|\vec{p}_0||\vec{p}_+| \cos \theta^{0+} , \\ T_1^0 = -4|\vec{p}_-||\vec{p}_0| \cos \theta^{-0} , \end{cases} \quad (18)$$

where  $\vec{p}_j, \vec{p}_k$  are the three momenta of the  $\pi^j$  and  $\pi^k$  in the rest frame of  $\rho^\kappa$  (or the  $\pi^i\pi^j$  system), and the  $\theta^{jk}(\equiv \theta_\kappa)$  is the angle between  $\vec{p}_j$  and  $\vec{p}_k$  (see Fig. 1).

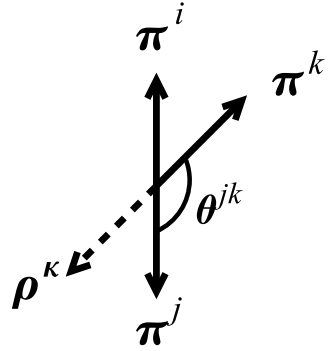


FIG. 1: The relation between three pions in the rest frame of  $\rho^\kappa$ .

### 1-5. Fitting parameters

Inserting (15), into expressions (13) and (14), the coefficients of equation (11) become

$$|A_{3\pi}|^2 \pm |\overline{A}_{3\pi}|^2 = \sum_{\kappa \in \{+,-,0\}} |f_\kappa|^2 U_\kappa^\pm + 2 \sum_{\kappa < \sigma \in \{+,-,0\}} (\text{Re}[f_\kappa f_\sigma^*] U_{\kappa\sigma}^{\pm, \text{Re}} - \text{Im}[f_\kappa f_\sigma^*] U_{\kappa\sigma}^{\pm, \text{Im}}) , \quad (19)$$

$$\text{Im} \left( \frac{q}{p} A_{3\pi}^* \overline{A}_{3\pi} \right) = \sum_{\kappa \in \{+,-,0\}} |f_\kappa|^2 I_\kappa + \sum_{\kappa < \sigma \in \{+,-,0\}} (\text{Re}[f_\kappa f_\sigma^*] I_{\kappa\sigma}^{\text{Im}} + \text{Im}[f_\kappa f_\sigma^*] I_{\kappa\sigma}^{\text{Re}}) , \quad (20)$$

with

$$U_\kappa^\pm = (|A^\kappa|^2 \pm |\overline{A}^\kappa|^2)/N , \quad (21)$$

$$U_{\kappa\sigma}^{\pm, \text{Re}(\text{Im})} = \text{Re}(\text{Im}) [\overline{A}^\kappa A^{\sigma*} \pm \overline{A}^\kappa \overline{A}^{\sigma*}] /N , \quad (22)$$

$$I_\kappa = \text{Im} [\overline{A}^\kappa A^{\kappa*}] /N , \quad (23)$$

$$I_{\kappa\sigma}^{\text{Re}} = \text{Re} [\overline{A}^\kappa A^{\sigma*} - \overline{A}^\sigma A^{\kappa*}] /N , \quad (24)$$

$$I_{\kappa\sigma}^{\text{Im}} = \text{Im} [\overline{A}^\kappa A^{\sigma*} + \overline{A}^\sigma A^{\kappa*}] /N , \quad (25)$$

where  $N$  is a normalization factor. The 27 coefficients (21)-(25) are the parameters determined by the fit. This parameterization allows us to describe the differential decay width as a linear combination of independent functions, whose coefficients are the fit parameters in a well behaved fit. We fix the overall normalization by requiring  $U_+^+ = 1$ , i.e., we use  $N = |A^+|^2 + |\bar{A}^+|^2$ . Thus, 26 of the 27 coefficients are free parameters in the fit.

### 1-6. Square Dalitz plot (SDP)

The signal and the continuum background  $e^+e^- \rightarrow q\bar{q}(q = u, d, s, c)$ , which is the dominant background in this analysis, populate the kinematic boundaries of the usual Dalitz plot as shown in Figs. 2 and 3. Since we model part of the Dalitz plot probability density function (PDF) with a binned histogram, the distribution concentrated in a narrow region is not easy to treat. We therefore apply the transformation

$$ds_+ds_- \rightarrow |\det \mathbf{J}|dm'd\theta' , \quad (26)$$

which defines the square Dalitz plot (SDP) [13]. The new coordinates are

$$m' \equiv \frac{1}{\pi} \arccos \left( 2 \frac{m_0 - m_0^{\min}}{m_0^{\max} - m_0^{\min}} - 1 \right) , \quad (27)$$

$$\theta' \equiv \frac{1}{\pi} \theta_0 \quad \left( = \frac{1}{\pi} \theta^{+-} \right) , \quad (28)$$

where  $m_0 = \sqrt{s_0}$ ,  $m_0^{\max} = m_{B^0} - m_{\pi^0}$  and  $m_0^{\min} = 2m_{\pi^+}$  are the kinematic limits of  $m_0$ , and  $\mathbf{J}$  is the Jacobian of the transformation. The determinant of the Jacobian is given by

$$|\det \mathbf{J}| = 4|\vec{p}_+||\vec{p}_0|m_0 \cdot \frac{m_0^{\max} - m_0^{\min}}{2} \pi \sin(\pi m') \cdot \pi \sin(\pi \theta') , \quad (29)$$

where  $\vec{p}_+$  and  $\vec{p}_0$  are the three momenta of  $\pi^+$  and  $\pi^0$  in the  $\pi^+\pi^-$  rest frame.

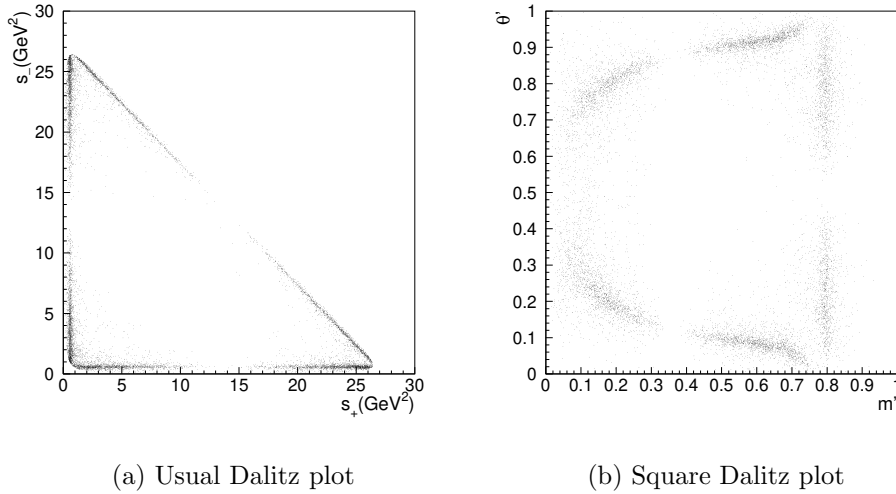


FIG. 2: Distribution of signal Monte Carlo (without detector efficiency and smearing) in the Dalitz plot.

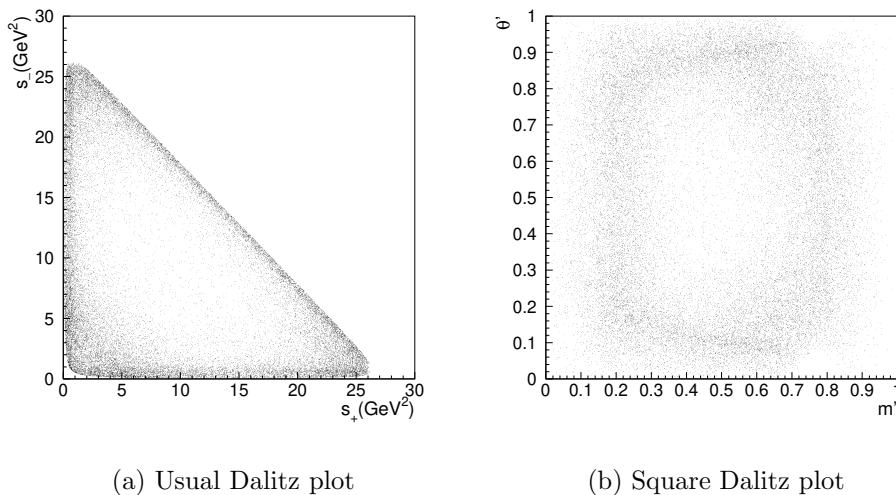


FIG. 3: Distribution of  $q\bar{q}$  background (from the data  $M_{bc}$  sideband) in the Dalitz plot.

## 2. EVENT SELECTION AND RECONSTRUCTION

To reconstruct candidate  $B^0 \rightarrow \pi^+\pi^-\pi^0$  decays, charged tracks reconstructed with the CDC and SVD are required to originate from the interaction point (IP) and to have transverse momenta greater than  $0.1 \text{ GeV}/c$ . We distinguish charged kaons from pions based on a kaon (pion) likelihood  $\mathcal{L}_{K(\pi)}$  derived from the TOF, ACC and  $dE/dx$  measurements in the CDC. Tracks that are positively identified as electrons are rejected.

Photons are identified as isolated ECL clusters that are not matched to any charged track. We reconstruct  $\pi^0$  candidates from pairs of photons detected in the barrel (end-cap) ECL with  $E_\gamma > 0.05$  ( $0.1$ ) GeV, where  $E_\gamma$  is the photon energy measured with the ECL. Photon pairs with momenta greater than  $0.1 \text{ GeV}/c$  in the laboratory frame and with an invariant mass between  $0.1178 \text{ GeV}/c^2$  to  $0.1502 \text{ GeV}/c^2$ , roughly corresponding to  $\pm 3\sigma$  of the mass resolution, are used as  $\pi^0$  candidates.

We identify  $B$  meson decays using the energy difference  $\Delta E \equiv E_B^{\text{cms}} - E_{\text{beam}}^{\text{cms}}$  and the beam-energy constrained mass  $M_{\text{bc}} \equiv \sqrt{(E_{\text{beam}}^{\text{cms}})^2 - (p_B^{\text{cms}})^2}$ , where  $E_{\text{beam}}^{\text{cms}}$  is the beam energy in the cms, and  $E_B^{\text{cms}}$  and  $p_B^{\text{cms}}$  are the cms energy and momentum of the reconstructed  $B$  candidate, respectively.

We select candidates in a fit region that is defined as  $-0.2 \text{ GeV} < \Delta E < 0.2 \text{ GeV}$  and  $5.2 \text{ GeV}/c^2 < M_{\text{bc}} < 5.3 \text{ GeV}/c^2$ . The fit region consists of the signal region that is defined as  $-0.1 \text{ GeV} < \Delta E < 0.08 \text{ GeV}$  and  $M_{\text{bc}} > 5.27 \text{ GeV}/c^2$ , and the complement, called the sideband region, which is dominated by background events.

The vertex position for the  $B^0 \rightarrow \pi^+\pi^-\pi^0$  decay is reconstructed using charged tracks that have enough SVD hits [14]. The  $f_{\text{tag}}$  vertex is obtained with well reconstructed tracks that are not assigned to  $f_{CP}$ . A constraint on the interaction-region profile in the plane perpendicular to the beam axis is also used with the selected tracks.

The  $b$ -flavor of the accompanying  $B$  meson is identified from inclusive properties of particles that are not associated with the reconstructed  $B^0 \rightarrow f_{CP}$  decay. We use two parameters, the  $b$ -flavor charge  $q_{\text{tag}}$  and  $r$ , to represent the tagging information [15]. The parameter  $r$  is an event-by-event, Monte Carlo (MC) determined flavor-tagging dilution factor that ranges from  $r = 0$  for no flavor discrimination to  $r = 1$  for unambiguous flavor assignment. It is used only to sort data into six  $r$  intervals. The wrong tag fractions for the six  $r$  intervals,  $w_l$  ( $l = 1, 6$ ), and differences between  $B^0$  and  $\bar{B}^0$  decays,  $\Delta w_l$ , are determined using a high-statistics control sample of semileptonic and hadronic  $b \rightarrow c$  decays [15, 16, 17].

The dominant background for the  $B^0 \rightarrow \pi^+\pi^-\pi^0$  signal comes from continuum events. To distinguish these jet-like events from the spherical  $B$  decay signal events, we combine a set of variables that characterize the event topology into a signal (background) likelihood variable  $\mathcal{L}_{\text{sig(bkg)}}$ , and impose requirements on the likelihood ratio  $\mathcal{R}_{\text{s/b}} \equiv \mathcal{L}_{\text{sig}}/(\mathcal{L}_{\text{sig}} + \mathcal{L}_{\text{bkg}})$  that depend on the quality of flavor tagging.

When more than one candidate in the same event is found in the fit region, we select the best candidate based on the reconstructed  $\pi^0$  mass and  $\mathcal{R}_{\text{s/b}}$ .

After the best candidate selection, we reconstruct the Dalitz variables  $s_+$ ,  $s_0$  and  $s_-$  from 1) the four momenta of the  $\pi^+$  and  $\pi^-$ , 2) the helicity angle of the  $\rho^0$  (i.e., the helicity angle of the  $\pi^+\pi^-$  system), and 3) the relation:  $m_{B^0}^2 + 2m_{\pi^+}^2 + m_{\pi^0}^2 = s_+ + s_- + s_0$ . Note that the energy of  $\pi^0$  is not explicitly used here, which improves the resolution of the Dalitz plot variables. We reject candidates that are located in one of the following regions in the Dalitz plot:  $\sqrt{s_0} > 0.95 \text{ GeV}/c^2$  and  $\sqrt{s_+} > 1.0 \text{ GeV}/c^2$  and  $\sqrt{s_-} > 1.0 \text{ GeV}/c^2$ ;  $\sqrt{s_0} < 0.55 \text{ GeV}/c^2$  or  $\sqrt{s_+} < 0.55 \text{ GeV}/c^2$  or  $\sqrt{s_-} < 0.55 \text{ GeV}/c^2$ . In these regions, the

fraction of  $B^0 \rightarrow \rho\pi$  signal is small. However, radial excitations ( $\rho(1450)$  and  $\rho(1700)$ ) are the dominant  $B^0 \rightarrow \pi^+\pi^-\pi^0$  contributions in the region with  $\sqrt{s} > 1.0 \text{ GeV}/c^2$ . Since the amplitudes of the radial excitations are in general independent of the amplitude of the  $\rho(770)$ , they are considered to be background in our analysis; vetoing the high mass region considerably reduces the systematic uncertainties due to their contributions.

Figure 4 shows the  $M_{bc}$  and  $\Delta E$  distributions for the reconstructed  $B^0 \rightarrow \pi^+\pi^-\pi^0$  candidates within the  $\Delta E$  and  $M_{bc}$  signal regions, respectively. The signal yield is determined from an unbinned four-dimensional extended-maximum-likelihood fit to the  $\Delta E$ - $M_{bc}$  and Dalitz plot distribution in the fit region defined as  $M_{bc} > 5.2 \text{ GeV}/c^2$  and  $-0.2 \text{ GeV} < \Delta E < 0.2 \text{ GeV}$ , where the Dalitz plot distribution is only used for the events inside the  $\Delta E$ - $M_{bc}$  signal region. The  $\Delta E$ - $M_{bc}$  distribution of signal is modeled with binned histograms obtained from MC, where the correlation between  $\Delta E$  and  $M_{bc}$ , the dependence on  $p_{\pi^0}$ , and the difference between data and MC are taken into account. We also take into account incorrectly reconstructed signal events, which we call self cross feed (SCF) and which amounts to  $\sim 20\%$  of the signal. In a SCF event, one of the three pions in  $f_{CP}$  is swapped with a pion in  $f_{tag}$  or the  $\pi^0$  in  $f_{CP}$  is misreconstructed. We give the details of the  $\Delta E$ - $M_{bc}$  and Dalitz plot PDFs of the SCF events in appendix A. For continuum, we use the ARGUS parameterization [18] for  $M_{bc}$  and a linear function for  $\Delta E$ . The  $\Delta E$ - $M_{bc}$  distribution of  $B\bar{B}$  background is modeled by binned histograms based on MC. The Dalitz plot distributions for all components are modeled in the same way as the time-dependent fit described later, but integrated over the dimensions of the proper time difference,  $\Delta t$ , and the flavor of the tag side  $B$ ,  $q_{tag}$ . The fit yields  $987 \pm 42$   $B^0 \rightarrow \pi^+\pi^-\pi^0$  events in the signal region, where the errors are statistical only.

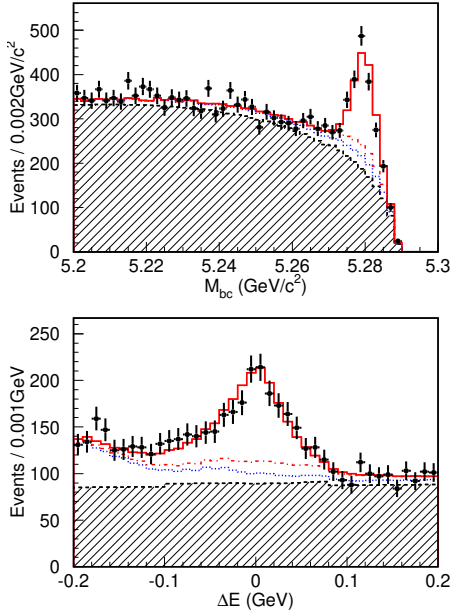


FIG. 4: The  $M_{bc}$ (upper) and  $\Delta E$ (lower) distributions within the  $\Delta E$  and  $M_{bc}$  signal regions. The histograms are cumulative. Solid, dot-dashed, dotted and dashed hatched histograms correspond to correctly reconstructed signal, SCF,  $B\bar{B}$ , and continuum PDFs, respectively.

### 3. DETERMINATION OF THE CONTRIBUTIONS FROM RADIAL EXCITATIONS

Using the same data sample as described above but performing a time-integrated Dalitz plot fit with a wider Dalitz plot acceptance,  $0.55 \text{ GeV}/c^2 < \sqrt{s_0} < 1.5 \text{ GeV}/c^2$  or  $\sqrt{s_+} < 1.5 \text{ GeV}/c^2$  or  $\sqrt{s_-} < 1.5 \text{ GeV}/c^2$ , we determine the  $\rho$  lineshape, i.e. the phases and amplitudes of the coefficients  $\beta$  and  $\gamma$  in equation (16), which we use for all of the decay amplitudes. In this fit, we use the PDG values [19] for the masses and widths of the  $\rho(1450)$  and  $\rho(1700)$ . The fit yields

$$|\beta| = 0.30^{+0.06}_{-0.05}, \quad \arg \beta = (213^{+15}_{-19})^\circ, \quad |\gamma| = 0.07 \pm 0.03, \quad \arg \gamma = (91^{+27}_{-32})^\circ. \quad (30)$$

The mass distributions and fit results are shown in Fig. 5. Figure 6 schematically shows how the radial excitations contribute to our fit result. Note that the values given above for  $\beta$  and  $\gamma$  and their errors are not meaningful measurements of physics parameters but rather are quantities needed for the time-dependent Dalitz fit. This is because these parameters are determined from the interference region, the interference between  $\rho^+ \pi^-$  and  $\rho^- \pi^+$ , etc., and depend on the unfounded common lineshape assumption of the equation (15). However, because statistics are still low, the time-dependent Dalitz analysis would not be possible if we were to discard the common lineshape assumption.

Thus, it is important to determine the common or *average* lineshape as well as obtain an upper limit on the deviation from the average lineshape for each of the 6 decay amplitudes. For this purpose, we put constraints on additional amplitudes that describe 1) the excess in the high mass region,  $\sqrt{s} > 0.9 \text{ GeV}/c^2$ , and 2) the interferences between radial excitations and the lowest resonance, the  $\rho(770)$ : interferences between  $\rho(770)^+ \pi^-$  and  $\rho(1450)^- \pi^+$ , etc. The nominal fit is performed with the average lineshape determined above, fixing all of the additional amplitudes to zero. When floating the additional amplitudes for the other resonances, we obtain results consistent with zero for all of the additional amplitudes but with large uncertainties compared to the errors for the average lineshape parameters above. We use the fit result with the additional lineshape parameters floating including their uncertainties in the systematic error study.

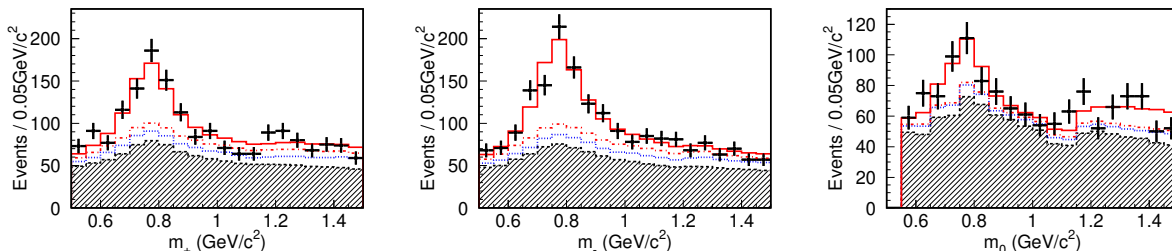


FIG. 5: Mass distributions and fitted lineshapes in  $\rho^+ \pi^-$  (left),  $\rho^- \pi^+$  (middle), and  $\rho^0 \pi^0$  (right) enhanced regions. The histograms are cumulative. Solid, dot-dashed, dotted and dashed hatched histograms correspond to correctly reconstructed signal, SCF,  $B\bar{B}$ , and continuum PDFs, respectively. Note that there are feed-downs from other quasi-two-body components than those of interest, especially in the high-mass regions. For example, the high-mass region ( $m_0 \gtrsim 1.0 \text{ GeV}/c^2$ ) of the  $\rho^0 \pi^0$  enhanced region (right) includes large contributions from  $\rho^\pm \pi^\mp$ .

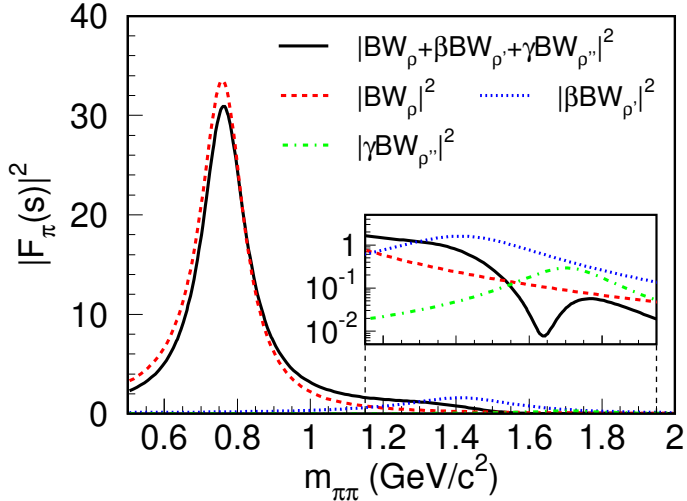


FIG. 6: A schematic figure of the fit result of the lineshape and the contributions from radial excitations. Note that our definition of  $F_\pi(s)$  does not include the factor  $1/(1 + \beta + \gamma)$  as in equation (16). One can see that the  $\rho(770)$  and  $\rho(1450)$  destructively interfere with each other near  $\sqrt{s} \equiv m_{\pi\pi} = 1.4(\text{GeV}/c^2)$ , which means that the  $\rho(1450)$  has a large impact on the phase of  $F_\pi(s)$  although the absolute value of  $|F_\pi(s)|$  is not much affected.

#### 4. TIME-DEPENDENT DALITZ PLOT ANALYSIS

To determine the 26 Dalitz plot parameters, we define the following event-by-event PDF:

$$\begin{aligned} p(\vec{x}) \equiv & f_{\text{sig}} p_{\text{sig}}^l(\Delta E, M_{\text{bc}}; m', \theta'; \Delta t, q_{\text{tag}}; p_{\pi^0}) \\ & + f_{BB} p_{BB}^l(\Delta E, M_{\text{bc}}; m', \theta'; \Delta t, q_{\text{tag}}) \\ & + f_{qq} p_{qq}^l(\Delta E, M_{\text{bc}}; m', \theta'; \Delta t, q_{\text{tag}}) , \end{aligned} \quad (31)$$

where  $p_{\text{sig}}^l$ ,  $p_{BB}^l$  and  $p_{qq}^l$  are PDF's for signal,  $B\bar{B}$  background and continuum background in flavor tagging region  $l$ , respectively, and  $f_{\text{sig}}$ ,  $f_{BB}$  and  $f_{qq}$  are the corresponding fractions that satisfy

$$f_{\text{sig}} + f_{BB} + f_{qq} = 1 . \quad (32)$$

The vector  $\vec{x}$ , the argument of  $p$ , corresponds to a set of event-by-event variables:

$$\vec{x} \equiv (\Delta E, M_{\text{bc}}; m', \theta'; \Delta t, q_{\text{tag}}, l; p_{\pi^0}) . \quad (33)$$

The PDF for signal events consists of a PDF for the correctly reconstructed events  $p_{\text{true}}^l$  and PDFs for SCF(Self Cross Feed) events  $p_i^l$  ( $i = \text{NR, CR}$ ):

$$p_{\text{sig}}^l = \frac{p_{\text{true}}^l(\Delta E, M_{\text{bc}}; m', \theta'; \Delta t, q_{\text{tag}}; p_{\pi^0}) + \sum_{i=\text{NR, CR}} p_i^l(\Delta E, M_{\text{bc}}; m', \theta'; \Delta t, q_{\text{tag}})}{n_{\text{true}} + \sum_{i=\text{NR, CR}} n_i} , \quad (34)$$

where NR and CR represent the  $\pi^0$  (neutral) replaced and  $\pi^\pm$  (charged) replaced SCF, respectively, and  $n$  are the integrals of the PDFs. A detailed description of the PDF for each component can be found in appendix A.

With the PDF defined above, we form the likelihood function

$$\mathcal{L} \equiv \prod_i p(\vec{x}_i) , \quad (35)$$

where  $i$  is an index over events. We perform an unbinned-maximum-likelihood fit and determine the 26 Dalitz plot parameters using the likelihood function with the signal fraction and the lineshape parameters obtained in Sec. 2 and Sec. 3, respectively.

## 5. FIT RESULT

A fit to the 2,824 events in the signal region yields the result listed in Table I. The correlation matrix of the 26 parameters after combining statistical and systematic errors is shown in the appendix B. Figure 7 shows the projections of the square Dalitz plot in data with the fit result superimposed. We also show the mass and helicity distribution for each  $\rho\pi$  enhanced region along with projections of the fit (Fig. 8). Figure 9 shows the  $\Delta t$  distributions and background subtracted asymmetries. We define the asymmetry in each  $\Delta t$  bin by  $(N_{q_{\text{tag}}=+1} - N_{q_{\text{tag}}=-1})/(N_{q_{\text{tag}}=+1} + N_{q_{\text{tag}}=-1})$ , where  $N_{q_{\text{tag}}=+1(-1)}$  corresponds the background subtracted number of events with  $q_{\text{tag}} = +1(-1)$ . The  $\rho^-\pi^+$  enhanced region shows a significant asymmetry, corresponding to a non-zero value of  $U_-^+$ .

### 5-1. Treatment of statistical errors

With a Toy MC study, we check the pull distribution, where the pull is defined as the residual divided by the MINOS error. Here, the MINOS error, which corresponds to the deviation from the best fit parameter when  $-2 \ln(\mathcal{L}/\mathcal{L}_{\max})$  is changed by one, is an estimate of the statistical error. Although the pull is expected to follow a Gaussian distribution with unit width, we find that the width of the pull distribution tends to be significantly larger than one for the interference terms due to small statistics. To restore the pull width to unity, we multiply the MINOS errors of the interference terms by a factor of 1.19, which is the average pull width for the interference terms obtained above, and quote the results as the statistical errors. For the non-interfering terms, we quote the MINOS errors without the correction factor.

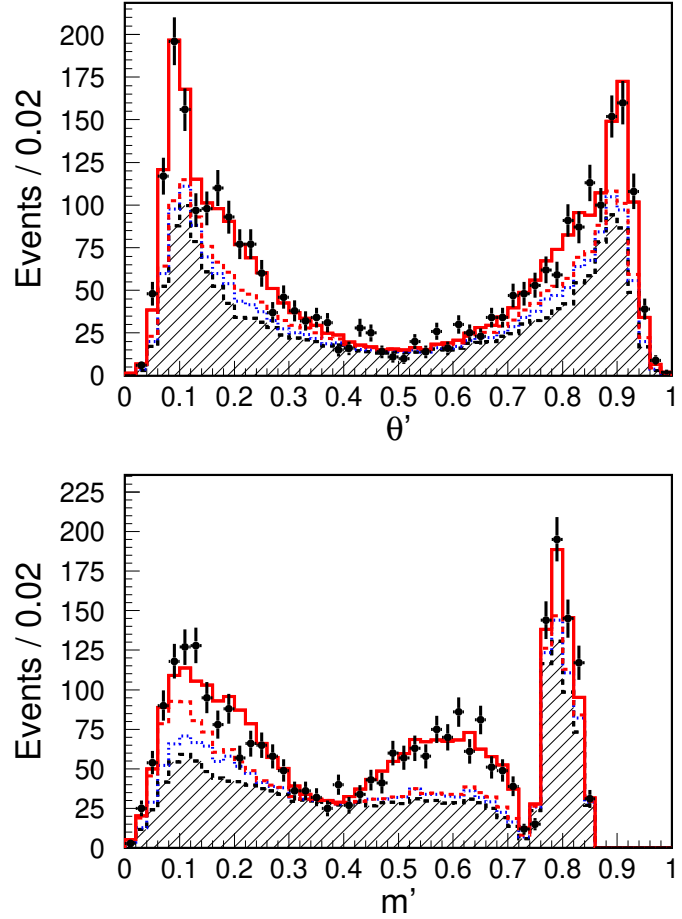


FIG. 7: Distributions of  $\theta'$  (upper) and  $m'$  (lower) with fit results. The histograms are cumulative. Solid, dot-dashed, dotted and dashed hatched histograms correspond to correctly reconstructed signal, SCF,  $B\bar{B}$ , and continuum PDFs, respectively.

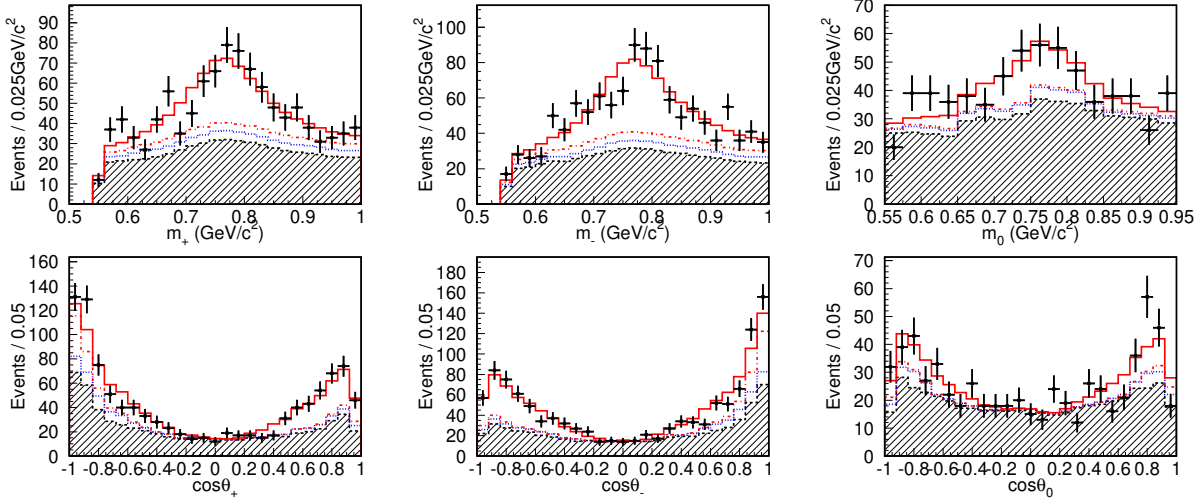


FIG. 8: Mass (upper) and helicity (lower) distribution of  $\rho^+\pi^-$  (left),  $\rho^-\pi^+$  (middle), and  $\rho^0\pi^0$  (right) enhanced regions. The histograms are cumulative. Solid, dot-dashed, dotted and dashed hatched histograms correspond to correctly reconstructed signal, SCF,  $B\bar{B}$ , and continuum PDFs, respectively.

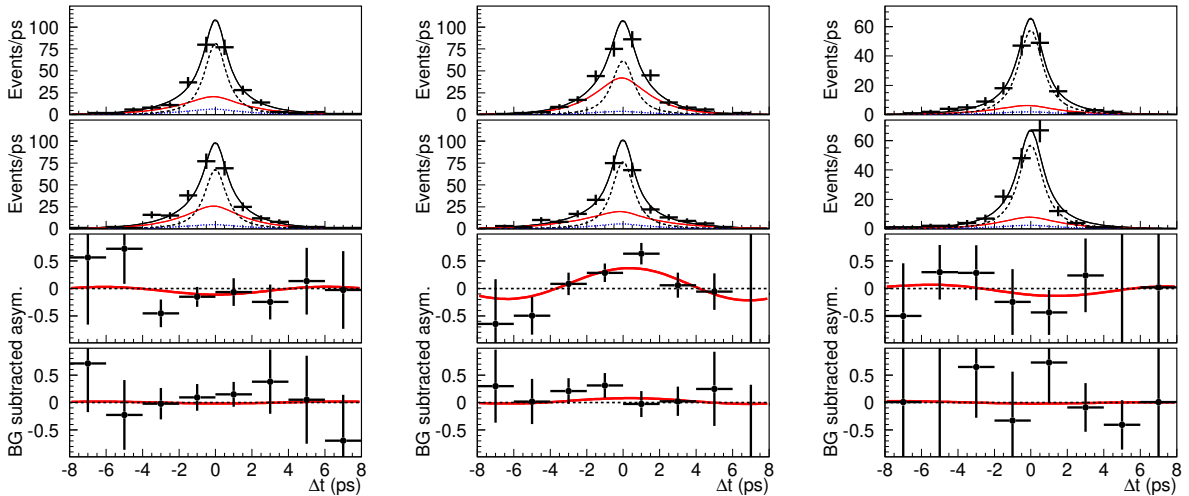


FIG. 9: Proper time distributions of good tag ( $r > 0.5$ ) regions for  $f_{\text{tag}} = B^0$  (upper) and  $f_{\text{tag}} = \bar{B}^0$  (middle upper), in  $\rho^+\pi^-$  (left),  $\rho^-\pi^+$  (middle),  $\rho^0\pi^0$  (right) enhanced regions, where solid (red), dotted, and dashed curves correspond to signal, continuum, and  $B\bar{B}$  PDFs. The middle lower and lower plots show the background subtracted asymmetries in the good tag ( $r > 0.5$ ) and poor tag ( $r < 0.5$ ) regions, respectively. The significant asymmetry in the  $\rho^-\pi^+$  enhanced region (middle) corresponds to a non-zero value of  $U_-^+$ .

TABLE I: Results of the time-dependent Dalitz fit.

	Fit Result
$U_+^+$	+1(fixed)
$U_-^+$	$+1.28 \pm 0.13(\text{stat.}) \pm 0.08(\text{syst.})$
$U_0^+$	$+0.30 \pm 0.06(\text{stat.}) \pm 0.05(\text{syst.})$
$U_{+-}^{\text{Re}}$	$+0.62 \pm 0.80(\text{stat.}) \pm 0.57(\text{syst.})$
$U_{+0}^{\text{Re}}$	$+0.41 \pm 0.52(\text{stat.}) \pm 0.46(\text{syst.})$
$U_{-0}^{\text{Re}}$	$+0.49 \pm 0.65(\text{stat.}) \pm 0.44(\text{syst.})$
$U_{+-}^{\text{Im}}$	$+0.86 \pm 0.83(\text{stat.}) \pm 0.49(\text{syst.})$
$U_{+0}^{\text{Im}}$	$-0.53 \pm 0.39(\text{stat.}) \pm 0.47(\text{syst.})$
$U_{-0}^{\text{Im}}$	$-1.72 \pm 0.69(\text{stat.}) \pm 0.53(\text{syst.})$
$U_+^-$	$+0.22 \pm 0.15(\text{stat.}) \pm 0.10(\text{syst.})$
$U_-^-$	$-0.62 \pm 0.17(\text{stat.}) \pm 0.09(\text{syst.})$
$U_0^-$	$+0.14 \pm 0.11(\text{stat.}) \pm 0.09(\text{syst.})$
$U_{+-}^{-\text{Re}}$	$-1.70 \pm 1.59(\text{stat.}) \pm 0.77(\text{syst.})$
$U_{+0}^{-\text{Re}}$	$-2.46 \pm 1.39(\text{stat.}) \pm 0.86(\text{syst.})$
$U_{-0}^{-\text{Re}}$	$-0.70 \pm 1.59(\text{stat.}) \pm 0.86(\text{syst.})$
$U_{+-}^{-\text{Im}}$	$-2.21 \pm 1.71(\text{stat.}) \pm 1.03(\text{syst.})$
$U_{+0}^{-\text{Im}}$	$-0.83 \pm 0.98(\text{stat.}) \pm 0.65(\text{syst.})$
$U_{-0}^{-\text{Im}}$	$-0.79 \pm 1.59(\text{stat.}) \pm 1.05(\text{syst.})$
$I_+^+$	$-0.03 \pm 0.11(\text{stat.}) \pm 0.06(\text{syst.})$
$I_-^+$	$+0.11 \pm 0.11(\text{stat.}) \pm 0.05(\text{syst.})$
$I_0^+$	$+0.02 \pm 0.09(\text{stat.}) \pm 0.06(\text{syst.})$
$I_{+-}^{\text{Re}}$	$+1.62 \pm 2.65(\text{stat.}) \pm 1.23(\text{syst.})$
$I_{+0}^{\text{Re}}$	$+1.45 \pm 2.41(\text{stat.}) \pm 1.12(\text{syst.})$
$I_{-0}^{\text{Re}}$	$-0.65 \pm 1.63(\text{stat.}) \pm 1.49(\text{syst.})$
$I_{+-}^{\text{Im}}$	$-1.76 \pm 2.42(\text{stat.}) \pm 1.31(\text{syst.})$
$I_{+0}^{\text{Im}}$	$+0.00 \pm 2.06(\text{stat.}) \pm 1.15(\text{syst.})$
$I_{-0}^{\text{Im}}$	$-2.58 \pm 1.72(\text{stat.}) \pm 1.33(\text{syst.})$

## 6. SYSTEMATIC UNCERTAINTIES

Tables II-IV list the systematic errors for the 26 time-dependent Dalitz plot parameters. The total systematic error is obtained by adding each source of systematic uncertainty in quadrature.

### 6-1. Radial excitations ( $\rho'$ and $\rho''$ )

The largest contribution for the interference terms tends to come from radial excitations. The systematic error related to the radial excitations ( $\rho(1450)$  and  $\rho(1700)$ , or  $\rho'$  and  $\rho''$ ) can be categorized into three classes: 1) uncertainties coming from the lineshape variation, i.e., the lineshape difference between each decay amplitude, 2) uncertainties in external parameters,  $m_{\rho(1450)}$ ,  $\Gamma_{\rho(1450)}$ ,  $m_{\rho(1700)}$ ,  $\Gamma_{\rho(1700)}$ , and 3) uncertainties in the common lineshape parameters  $\beta$  and  $\gamma$  used for the nominal fit.

In our nominal fit, we assume all of 6 decay amplitudes have the same contribution from  $\rho(1450)$  and  $\rho(1700)$ , i.e., we assume equation (15). This assumption, however, is not well grounded. In general, the contributions from  $\rho(1450)$  and  $\rho(1700)$  can be different for each of the decay amplitudes and thus the systematic uncertainty from this assumption must be addressed. Without the assumption about the higher resonances, equation (15) becomes

$$f_{\kappa}^{(-)} = T_1^{\kappa} F_{\pi}^{(-)}(s_{\kappa}), \quad (36)$$

where

$$F_{\pi}^{(-)}(s) \equiv BW_{\rho(770)}^{GS}(s) + (\beta + \Delta\beta_{\kappa})BW_{\rho(1450)}^{GS}(s) + (\gamma + \Delta\gamma_{\kappa})BW_{\rho(1700)}^{GS}(s). \quad (37)$$

The variation of the contributions from radial excitations is described by non-zero  $\Delta\beta_{\kappa}$  and  $\Delta\gamma_{\kappa}$ , which are 12 complex variables. We generate various Toy MC samples, where the input  $A^{\kappa}$  and  $\bar{A}^{\kappa}$  are fixed but the values of  $\Delta\beta_{\kappa}$  and  $\Delta\gamma_{\kappa}$  are randomly varied according to the constraints on  $\Delta\beta_{\kappa}$  and  $\Delta\gamma_{\kappa}$ ; these constraints are obtained from the results in Sec. 3, and are combined with the isospin relation [7, 8], which improves the constraints. The statistics for each pseudo-experiment are set to be large enough so that the statistical uncertainty is negligible. We assign the variations and the biases of the fit results due to the  $\Delta\beta_{\kappa}$  and  $\Delta\gamma_{\kappa}$  variation as systematic errors.

For the masses and widths of the  $\rho(1450)$  and  $\rho(1700)$ , we quote the values from the PDG [19]. To estimate the systematic error coming from uncertainties in their parameters, we generate Toy MC varying the input masses and widths and fit them with the masses and widths of the nominal fit. Here, we vary the masses by two times the PDG error ( $\pm 50 \text{ MeV}/c^2$  for  $\rho(1450)$  and  $\pm 40 \text{ MeV}/c^2$  for  $\rho(1700)$ ) since the variations between independent experiments are much larger than the  $1\sigma$  PDG errors, while we vary the widths by the  $\pm 1\sigma$  PDG errors. We quote the mean shift of the Toy MC ensemble as the systematic errors. We also take into account the systematic errors from the uncertainties in  $\beta$  and  $\gamma$  for the nominal fit (equation (30)) in the same way.

## 6-2. SCF

Systematic errors due to SCF are dominated by the uncertainty in the difference between data and MC; these errors are determined from the  $B \rightarrow D^{(*)}\rho$  control samples that contain a single  $\pi^0$  in the final state. We vary the amount of SCF by its  $1\sigma$  error, which is  $\pm 100\%$  for the CR SCF and  $^{+30(60)}_{-30}\%$  for the NR SCF in the DS-I(DS-II); we quote the difference from the nominal fit as the systematic error. The event fraction for each  $r$  region (for CR and NR), the wrong tag fractions (for CR) and lifetime used in the  $\Delta t$  PDF (for CR), which are obtained from MC, are also varied and the difference in the fit results is assigned as systematic error.

## 6-3. Signal Dalitz PDF

Systematic errors due to the Dalitz PDF for signal is mainly from the Dalitz plot dependent efficiency. We take account of MC statistics in the efficiency and uncertainty in the  $\pi^0$  momentum dependent efficiency correction,  $\epsilon'(p_{\pi^0})$ , obtained from the control samples of the decay modes  $\bar{B}^0 \rightarrow \rho^- D^{(*)+}$ ,  $\bar{B}^0 \rightarrow \pi^- D^{(*)+}$ ,  $B^- \rightarrow \rho^- D^{(*)0}$  and  $B^- \rightarrow \pi^- D^{(*)0}$ . The Dalitz plot efficiency obtained from MC is found to have a small charge asymmetry ( $\sim 3\%$  at most). We use this asymmetric efficiency for our nominal fit. To estimate the systematic error from the asymmetry, we fit the data using a symmetric efficiency and quote twice the difference between symmetric and asymmetric efficiencies as the systematic error. The Dalitz plot efficiency is  $r$  region dependent and obtained as a product with the event fraction in the corresponding region,  $\mathcal{F}_{\text{sig}}^l \cdot \epsilon'(m', \theta')$ , using MC. The difference in the fraction for data and MC is estimated to be  $\sim 10\%$  using the  $B^0 \rightarrow D^{*-} \pi^+$  decay mode as a control sample. The fractions are varied by  $\pm 10\%$  to estimate the systematic error.

## 6-4. Background Dalitz PDF

The Dalitz plot for continuum background has an uncertainty due to the limited statistics of the sideband events, which we use to model the PDF. We estimate the uncertainty by performing a Toy MC study of sideband events. With each pseudo-experiment, we model the PDF in the same way as we do for real data; with the PDF, we fit the data in the signal region; and we quote the variation of fit results as the systematic error. The flavor-asymmetry parameters of the continuum background, which are fitted from sideband events, are varied by their uncertainties. Systematic uncertainty from the statistics of the  $B\bar{B}$  MC, which is used to model the  $B\bar{B}$  Dalitz plot PDF, is also taken into account.

## 6-5. $B^0 \rightarrow \pi^+ \pi^- \pi^0$ processes other than $B^0 \rightarrow (\rho\pi)^0$

The primary contribution to the systematic errors of the non-interfering parameters tends to come from the  $B^0 \rightarrow \pi^+ \pi^- \pi^0$  decay processes that are not  $B^0 \rightarrow (\rho\pi)^0$ . We take account of the contributions from  $B^0 \rightarrow f_0(980)\pi^0$ ,  $B^0 \rightarrow f_0(600)\pi^0$ ,  $B^0 \rightarrow \omega\pi^0$ , and non-resonant  $B^0 \rightarrow \pi^+ \pi^- \pi^0$ . Upper limits on their contributions are determined from data, except for  $B^0 \rightarrow \omega\pi^0$ , for which we use the world average of  $\mathcal{B}(B^0 \rightarrow \omega\pi^0)$  [20] and  $\mathcal{B}(\omega \rightarrow \pi^+ \pi^-)$  [19]. For the mass and width parameters of the  $f_0(600)$  resonance, we use

recent measurements by BES [21], CLEO [22], and E791 [23] and take the largest variation. We find no significant signals for any of the above decay modes. Using the  $1\sigma$  upper limits as input, we generate Toy MC for each mode with the interference between the  $B^0 \rightarrow (\rho\pi)^0$  and the other  $B^0 \rightarrow \pi^+\pi^-\pi^0$  mode taken into account. We obtain the systematic error by fitting the Toy MC assuming  $B^0 \rightarrow (\rho\pi)^0$  only in the PDF. Within physically allowed regions, we vary the  $CP$  violation parameters of the other  $B^0 \rightarrow \pi^+\pi^-\pi^0$  modes and the relative phase difference between  $B^0 \rightarrow (\rho\pi)^0$  and the other  $B^0 \rightarrow \pi^+\pi^-\pi^0$  as the input parameters, and use the largest deviation as the systematic error for each decay mode.

### 6-6. Background fraction

Systematic errors due to the event-by-event  $\Delta E$ - $M_{bc}$  background fractions are studied by varying the PDF shape parameters and the fraction of continuum background, and the correction factor to the signal PDF shape by  $\pm 1\sigma$ . We also vary the fractions of the  $B\bar{B}$  background, which are estimated with MC, by  $\pm 50\%$  ( $\pm 20\%$ ) for the  $b \rightarrow c$  ( $b \rightarrow u$ ) transition.

### 6-7. Physics parameters

We use the world average [19, 20] for the following physics parameters:  $\tau_{B^0}$  and  $\Delta m_d$  (used for signal and  $B\bar{B}$  background  $\Delta t$ ), the CKM angles of  $\phi_1$  and  $\phi_2$  (used in  $B\bar{B}$  background), and the branching fractions of  $b \rightarrow u$  decay modes (used in  $B\bar{B}$  background). The systematic error is assigned by varying them by  $\pm 1\sigma$ . The charge asymmetry of  $B^0 \rightarrow a_1^\pm \pi^\mp$ , for which there is no measurement and we use zero in the nominal fit, is varied in the physically allowed region, i.e.,  $\pm 1$ .

### 6-8. Background $\Delta t$ PDF

Systematic errors from uncertainties in the background  $\Delta t$  shapes for both continuum and  $B\bar{B}$  backgrounds are estimated by varying each parameter by  $\pm 1\sigma$ .

### 6-9. Vertex reconstruction

To determine the systematic error that arises from uncertainties in the vertex reconstruction, the track and vertex selection criteria are varied to search for possible systematic biases. Systematic error due to the IP constraint in the vertex reconstruction is estimated by varying the smearing used to account for the  $B$  flight length by  $\pm 10 \mu m$ .

### 6-10. Resolution function for the $\Delta t$ PDF

Systematic errors due to uncertainties in the resolution function are estimated by varying each resolution parameter obtained from data (MC) by  $\pm 1\sigma$  ( $\pm 2\sigma$ ). Systematic errors due to uncertainties in the wrong tag fractions are also studied by varying the wrong tag fraction individually for each  $r$  region.

### 6-11. Fit bias

We observed fit bias due to small statistics for some of the fitted parameters. Since this bias is much smaller than the statistical error, we take it into account in the systematic errors. We estimate the size of the fit bias by Toy MC study and quote the bias as the systematic errors. We also confirm that the bias is consistent between Toy MC and full detector MC simulation.

### 6-12. Tag-side interference

Finally, we investigate the effects of tag-side interference (TSI), which is the interference between CKM-favored and CKM-suppressed  $B \rightarrow D$  transitions in the  $f_{\text{tag}}$  final state [24]. A small correction to the PDF for the signal distribution arises from the interference. We estimate the size of the correction using the  $B^0 \rightarrow D^* - \ell^+ \nu$  sample. We then generate MC pseudo-experiments and make an ensemble test to obtain the systematic biases.

TABLE II: Table of systematic errors (1). The notation “ $< 0.01$ ” means that the value is small and less than 0.01, and thus invisible in the number of significant digits shown here. We calculate the total systematic error including these small contributions.

	$U_-^+$	$U_0^+$	$U_{+-}^{+, \text{Re}}$	$U_{+0}^{+, \text{Re}}$	$U_{-0}^{+, \text{Re}}$	$U_{+-}^{+, \text{Im}}$	$U_{+0}^{+, \text{Im}}$	$U_{-0}^{+, \text{Im}}$
$\rho'$ and $\rho''$	0.01	0.01	0.29	0.19	0.26	0.32	0.37	0.29
SCF	0.01	0.02	0.31	0.14	0.17	0.03	0.03	0.10
Signal Dalitz	0.02	0.01	0.24	0.15	0.19	0.13	0.06	0.13
BG Dalitz	0.02	0.01	0.16	0.12	0.14	0.14	0.12	0.22
Other $\pi\pi\pi$	0.06	0.03	0.10	0.08	0.10	0.15	0.10	0.08
BG fraction	0.03	0.02	0.14	0.19	0.13	0.23	0.07	0.22
Physics	0.02	$< 0.01$	0.01	0.02	0.02	0.01	0.01	0.02
BG $\Delta t$	$< 0.01$	$< 0.01$	0.03	0.01	0.02	0.02	0.01	0.02
Vertexing	0.02	0.02	0.02	0.16	0.11	0.08	0.08	0.09
Resolution	$< 0.01$	$< 0.01$	0.04	0.07	0.03	0.04	0.03	0.02
Flavor tagging	$< 0.01$	$< 0.01$	$< 0.01$	$< 0.01$	0.01	$< 0.01$	$< 0.01$	0.01
Fit bias	0.01	0.01	0.16	0.22	0.07	0.09	0.22	0.24
TSI	$< 0.01$	$< 0.01$	0.01	0.01	0.01	0.03	0.01	0.01
Total	0.08	0.05	0.57	0.46	0.44	0.49	0.47	0.53

TABLE III: Table of systematic errors (2). The notation “ $< 0.01$ ” means that the value is small and less than 0.01, and thus invisible in the number of significant digits shown here. We calculate the total systematic error including these small contributions.

	$U_+^-$	$U_-^-$	$U_0^-$	$U_{+-}^{-,\text{Re}}$	$U_{+0}^{-,\text{Re}}$	$U_{-0}^{-,\text{Re}}$	$U_{+-}^{-,\text{Im}}$	$U_{+0}^{-,\text{Im}}$	$U_{-0}^{-,\text{Im}}$
$\rho'$ and $\rho''$	0.02	0.02	0.05	0.42	0.31	0.41	0.77	0.45	0.36
SCF	0.02	0.03	0.03	0.29	0.27	0.32	0.09	0.25	0.17
Signal Dalitz	0.01	0.02	0.02	0.28	0.32	0.32	0.38	0.15	0.53
BG Dalitz	0.04	0.03	0.02	0.29	0.36	0.30	0.31	0.22	0.41
Other $\pi\pi\pi$	0.05	0.05	0.03	0.12	0.11	0.14	0.15	0.11	0.13
BG fraction	0.03	0.04	0.02	0.31	0.30	0.32	0.38	0.22	0.49
Physics	0.01	0.01	$< 0.01$	0.04	0.03	0.04	0.04	0.02	0.06
BG $\Delta t$	$< 0.01$	$< 0.01$	$< 0.01$	0.03	0.04	0.02	0.04	0.02	0.05
Vertexing	0.04	0.02	0.05	0.17	0.45	0.16	0.08	0.10	0.27
Resolution	0.01	0.01	0.01	0.16	0.17	0.32	0.11	0.10	0.29
Flavor tagging	0.01	0.01	$< 0.01$	0.03	0.04	0.04	0.05	0.03	0.03
Fit bias	0.01	0.03	$< 0.01$	0.05	0.07	0.12	0.18	0.02	0.23
TSI	0.04	0.04	0.01	0.05	0.07	0.03	0.02	0.06	0.01
Total	0.10	0.09	0.09	0.77	0.86	0.86	1.03	0.65	1.05

TABLE IV: Table of systematic errors (3). The notation “ $< 0.01$ ” means that the value is small and less than 0.01, and thus invisible in the number of significant digits shown here. We calculate the total systematic error including these small contributions.

	$I_+$	$I_-$	$I_0$	$I_{+-}^{\text{Re}}$	$I_{+0}^{\text{Re}}$	$I_{-0}^{\text{Re}}$	$I_{+-}^{\text{Im}}$	$I_{+0}^{\text{Im}}$	$I_{-0}^{\text{Im}}$
$\rho'$ and $\rho''$	0.03	0.02	0.04	0.95	0.59	1.32	0.89	0.84	0.89
SCF	0.01	0.01	0.01	0.09	0.64	0.07	0.50	0.08	0.65
Signal Dalitz	0.01	0.01	0.01	0.33	0.29	0.30	0.31	0.35	0.31
BG Dalitz	0.01	0.01	0.01	0.34	0.38	0.30	0.32	0.34	0.33
Other $\pi\pi\pi$	0.03	0.03	0.02	0.17	0.15	0.18	0.22	0.15	0.20
BG frac.	0.02	0.01	0.01	0.44	0.34	0.33	0.32	0.37	0.29
Physics	0.01	0.01	$< 0.01$	0.05	0.06	0.03	0.05	0.05	0.05
BG $\Delta t$	$< 0.01$	$< 0.01$	$< 0.01$	0.05	0.04	0.04	0.05	0.04	0.11
Vertexing	0.02	0.02	0.04	0.16	0.28	0.14	0.42	0.37	0.28
Resolution	0.01	0.01	0.01	0.30	0.21	0.18	0.35	0.25	0.28
Flavor tagging	$< 0.01$	$< 0.01$	$< 0.01$	0.04	0.07	0.04	0.03	0.07	0.03
Fit bias	$< 0.01$	0.01	$< 0.01$	0.12	0.01	0.27	0.09	0.09	0.22
TSI	0.01	$< 0.01$	0.01	0.09	0.07	0.04	0.04	0.03	0.07
Total	0.06	0.05	0.06	1.23	1.12	1.49	1.31	1.15	1.33

TABLE V: Correlation matrix of the quasi-two-body parameters, with statistical and systematic error combined.

	$\mathcal{A}_{\rho\pi}^{CP}$	$\mathcal{C}$	$\Delta\mathcal{C}$	$\mathcal{S}$	$\Delta\mathcal{S}$
$\mathcal{A}_{\rho\pi}^{CP}$	+1.00				
$\mathcal{C}$	-0.15	+1.00			
$\Delta\mathcal{C}$	+0.08	+0.19	+1.00		
$\mathcal{S}$	+0.02	-0.02	-0.00	+1.00	
$\Delta\mathcal{S}$	-0.02	-0.00	-0.01	+0.30	+1.00

## 7. QUASI-TWO-BODY PARAMETERS

We calculate quasi-two-body  $CP$  violation parameters as

$$\mathcal{C}^+ = \frac{U_+^-}{U_+^+}, \quad \mathcal{C}^- = \frac{U_-^-}{U_-^+}, \quad \mathcal{S}^+ = \frac{2I_+}{U_+^+}, \quad \mathcal{S}^- = \frac{2I_-}{U_-^+}, \quad \mathcal{A}_{\rho\pi}^{CP} = \frac{U_+^+ - U_-^+}{U_+^+ + U_-^+}, \quad (38)$$

and

$$\mathcal{C} \equiv \frac{\mathcal{C}^+ + \mathcal{C}^-}{2}, \quad \Delta\mathcal{C} \equiv \frac{\mathcal{C}^+ - \mathcal{C}^-}{2}, \quad \mathcal{S} \equiv \frac{\mathcal{S}^+ + \mathcal{S}^-}{2}, \quad \Delta\mathcal{S} \equiv \frac{\mathcal{S}^+ - \mathcal{S}^-}{2}. \quad (39)$$

We obtain

$$\mathcal{A}_{\rho\pi}^{CP} = -0.12 \pm 0.05 \pm 0.03, \quad (40)$$

$$\mathcal{C} = -0.13 \pm 0.09 \pm 0.06, \quad (41)$$

$$\Delta\mathcal{C} = +0.35 \pm 0.10 \pm 0.06, \quad (42)$$

$$\mathcal{S} = +0.06 \pm 0.13 \pm 0.07, \quad (43)$$

$$\Delta\mathcal{S} = -0.12 \pm 0.14 \pm 0.07, \quad (44)$$

where first errors and second errors are statistical and systematic, respectively. The correlation matrix is shown in Table V.

One can transform the parameters into the direct  $CP$  violation parameters  $\mathcal{A}_{\rho\pi}^{+-}$  and  $\mathcal{A}_{\rho\pi}^{-+}$  defined as

$$\mathcal{A}_{\rho\pi}^{+-} \equiv -\frac{\mathcal{A}_{\rho\pi}^{CP} + \mathcal{C} + \mathcal{A}_{\rho\pi}^{CP}\Delta\mathcal{C}}{1 + \Delta\mathcal{C} + \mathcal{A}_{\rho\pi}^{CP}\mathcal{C}}, \quad (45)$$

$$\mathcal{A}_{\rho\pi}^{-+} \equiv \frac{\mathcal{A}_{\rho\pi}^{CP} - \mathcal{C} - \mathcal{A}_{\rho\pi}^{CP}\Delta\mathcal{C}}{1 - \Delta\mathcal{C} - \mathcal{A}_{\rho\pi}^{CP}\mathcal{C}}, \quad (46)$$

which can be more convenient for interpretation. We obtain

$$\mathcal{A}_{\rho\pi}^{+-} = +0.22 \pm 0.08 \pm 0.05, \quad (47)$$

$$\mathcal{A}_{\rho\pi}^{-+} = +0.08 \pm 0.17 \pm 0.12, \quad (48)$$

with a correlation coefficient of +0.53. Our result differs from the case with no direct  $CP$  asymmetry ( $\mathcal{A}_{\rho\pi}^{+-} = 0$  and  $\mathcal{A}_{\rho\pi}^{-+} = 0$ ) by 2.4 standard deviations (Fig. 10). Measurements with a larger data sample may be needed to observe direct  $CP$  violation.

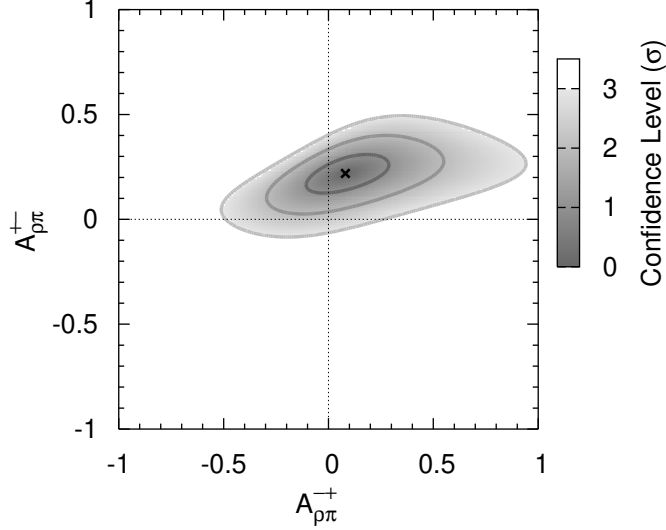


FIG. 10: Contour plot of the confidence level for the direct  $CP$  violation parameters  $\mathcal{A}_{\rho\pi}^{+-}$  vs.  $\mathcal{A}_{\rho\pi}^{-+}$ .

The ratio of the branching fractions  $\mathcal{B}(B^0 \rightarrow \rho^0 \pi^0)/\mathcal{B}(B^0 \rightarrow \rho^\pm \pi^\mp)$  can be related to our measurement as

$$\frac{\mathcal{B}(B^0 \rightarrow \rho^0 \pi^0)}{\mathcal{B}(B^0 \rightarrow \rho^\pm \pi^\mp)} = \frac{U_0^+}{U_+^+ + U_-^+} . \quad (49)$$

Our measurement yields

$$\frac{\mathcal{B}(B^0 \rightarrow \rho^0 \pi^0)}{\mathcal{B}(B^0 \rightarrow \rho^\pm \pi^\mp)} = 0.133 \pm 0.022 \pm 0.023 . \quad (50)$$

This is consistent with the dedicated quasi-two-body branching fraction measurement of  $B^0 \rightarrow \rho^0 \pi^0$  from Belle [25]:

$$\frac{\mathcal{B}(B^0 \rightarrow \rho^0 \pi^0)^{\text{Belle}}}{\mathcal{B}(B^0 \rightarrow \rho^\pm \pi^\mp)^{\text{WA}}} = \frac{3.12^{+0.88+0.60}_{-0.82-0.76}}{24.0 \pm 2.5} = 0.130^{+0.049}_{-0.046} , \quad (51)$$

where we use the world average [20] for the denominator.

We also measure the  $CP$  violating parameters of  $B^0 \rightarrow \rho^0 \pi^0$  calculated as

$$\mathcal{A}_{\rho^0 \pi^0} = -\frac{U_0^-}{U_0^+} , \quad \mathcal{S}_{\rho^0 \pi^0} = \frac{2I_0}{U_0^+} . \quad (52)$$

We obtain

$$\mathcal{A}_{\rho^0 \pi^0} = -0.45 \pm 0.35 \pm 0.32 , \quad (53)$$

$$\mathcal{S}_{\rho^0 \pi^0} = +0.15 \pm 0.57 \pm 0.43 , \quad (54)$$

with correlation coefficient of  $-0.07$ . Our measurement of  $\mathcal{A}_{\rho^0 \pi^0}$  is consistent with the previous measurement from Belle [25]. This is the first measurement of  $\mathcal{S}_{\rho^0 \pi^0}$ .

## 8. CONSTRAINT ON THE CKM ANGLE $\phi_2$

We constrain the CKM angle  $\phi_2$  from our analysis following the procedure described in Ref. [6]. With three  $B^0 \rightarrow (\rho\pi)^0$  decay modes, we have 9 free parameters including  $\phi_2$ :

$$9 = (6 \text{ complex amplitudes} = 12 \text{ d.o.f.}) + \phi_2 \\ - (1 \text{ global phase}) - (1 \text{ global normalization}) - (1 \text{ isospin relation} = 2 \text{ d.o.f.}), \quad (55)$$

where we make use of an isospin relation that relates neutral  $B$  decay processes only [7, 8]. Parameterizing the 6 complex amplitudes with 9 free parameters, we form a  $\chi^2$  function using the 26 measurements of our time-dependent Dalitz plot analysis as constraints. We first optimize all the 9 parameters to obtain a minimum  $\chi^2$ ,  $\chi^2_{\min}$ ; we then scan  $\phi_2$  from  $0^\circ$  to  $180^\circ$  optimizing the other 8 parameters, whose resultant minima are defined as  $\chi^2(\phi_2)$ ; and  $\Delta\chi^2(\phi_2)$  is defined as  $\Delta\chi^2(\phi_2) \equiv \chi^2(\phi_2) - \chi^2_{\min}$ . Performing a Toy MC study following the procedure described in Ref. [26], we obtain the 1 – C.L. plot in Fig. 11 from the  $\Delta\chi^2(\phi_2)$ [28].

In addition to the 26 observables obtained from our time-dependent Dalitz plot analysis, we use the following world average branching fractions and asymmetries:  $\mathcal{B}(B^0 \rightarrow \rho^\pm\pi^\mp)$ ,  $\mathcal{B}(B^+ \rightarrow \rho^+\pi^0)$ ,  $\mathcal{A}(B^+ \rightarrow \rho^+\pi^0)$ ,  $\mathcal{B}(B^+ \rightarrow \rho^0\pi^+)$ , and  $\mathcal{A}(B^+ \rightarrow \rho^0\pi^+)$  [20], which are not correlated with our 26 observables. With the 31 measurements above, we perform a full combined Dalitz and isospin(pentagon) analysis. Having 5 related decay modes, we have 12 free parameters including  $\phi_2$ :

$$12 = (10 \text{ complex amplitudes} = 20 \text{ d.o.f.}) + \phi_2 \\ - (1 \text{ global phase}) - (4 \text{ isospin relations} = 8 \text{ d.o.f.}). \quad (56)$$

The detail of  $\chi^2$  formation can be found in appendix C. The  $\chi^2_{\min}$  obtained is 9.8, which is reasonable for  $31(\text{measurements}) - 12(\text{free parameters}) = 19$  degrees of freedom. Following the same procedure as above, we obtain the 1 – C.L. plot in the Fig. 12. We obtain  $\phi_2 = (83^{+12}_{-23})^\circ$  as the central value and  $1\sigma$  errors (corresponding to 68.3% C.L.). A large CKM-disfavored region ( $\phi_2 < 8^\circ$  and  $129^\circ < \phi_2$ ) also remains.

## 9. CONCLUSION

We have performed a full Dalitz plot analysis of the  $B^0 \rightarrow \pi^+\pi^-\pi^0$  decay mode. The results are consistent with no direct  $CP$  violation and the previous measurement of  $B^0 \rightarrow \rho^0\pi^0$  branching fraction and flavor asymmetry. Combining our analysis and information from charged  $B$  decay modes, a full Dalitz plot and isospin analysis is performed to obtain a constraint on  $\phi_2$ . We obtain  $\phi_2 = (83^{+12}_{-23})^\circ$  as the central value with  $1\sigma$  errors. However, a large CKM-disfavored region ( $\phi_2 < 8^\circ$  and  $129^\circ < \phi_2$ ) also remains. In principle, with more data we may be able to remove the additional  $\phi_2$  solutions.

### Acknowledgment

We thank the KEKB group for the excellent operation of the accelerator, the KEK cryogenics group for the efficient operation of the solenoid, and the KEK computer group and the National Institute of Informatics for valuable computing and Super-SINET network support. We acknowledge support from the Ministry of Education, Culture, Sports, Science,

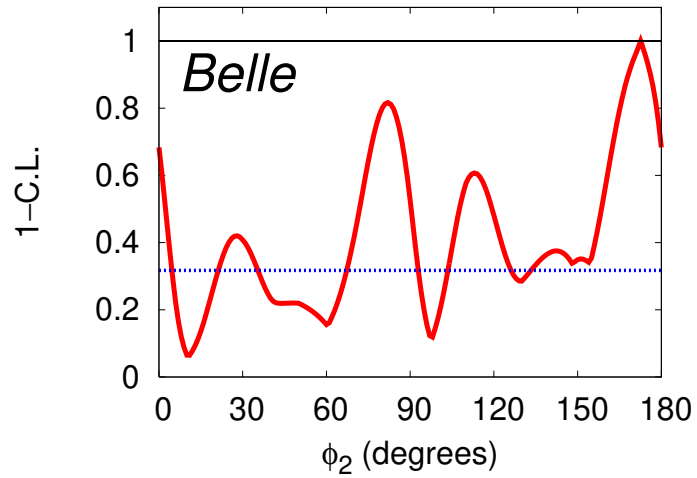


FIG. 11:  $1 - \text{C.L.}$  vs.  $\phi_2$  obtained by Dalitz analysis. The dotted horizontal line corresponds to the  $1\sigma$  confidence level.

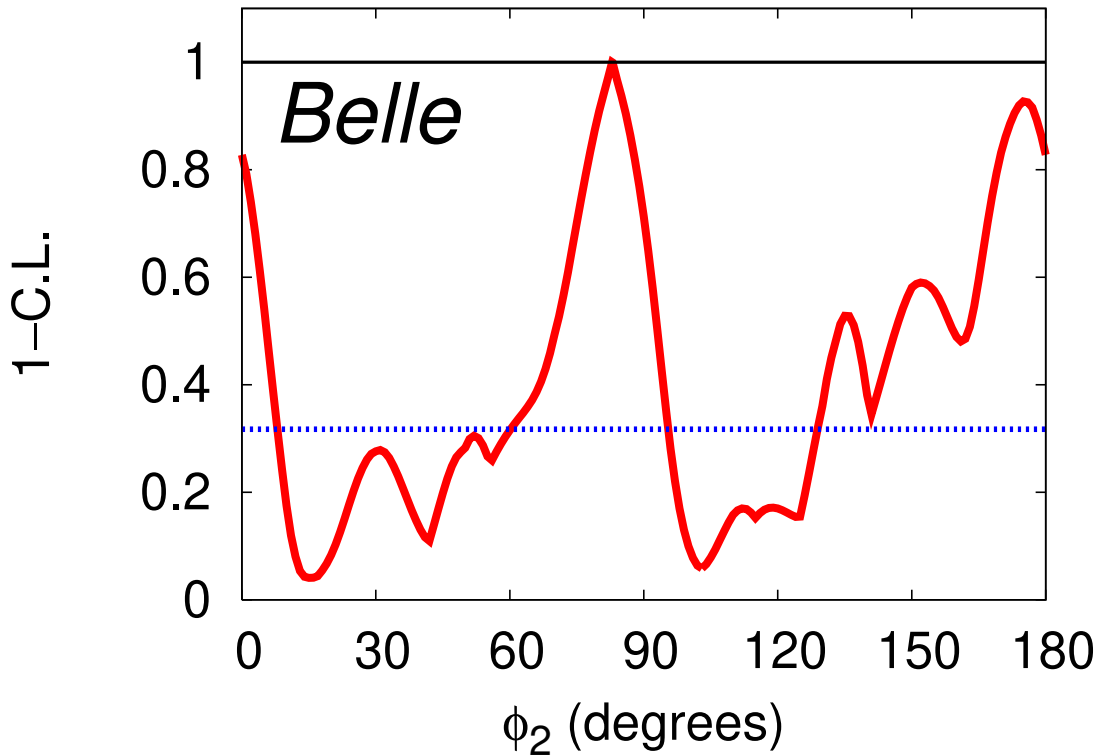


FIG. 12:  $1 - \text{C.L.}$  vs.  $\phi_2$  obtained by a full combined Dalitz and isospin(pentagon) analysis. The dotted horizontal line corresponds to the  $1\sigma$  confidence level.

and Technology of Japan and the Japan Society for the Promotion of Science; the Australian Research Council and the Australian Department of Education, Science and Training; the National Science Foundation of China and the Knowledge Innovation Program of the Chinese Academy of Sciences under contract No. 10575109 and IHEP-U-503; the Department of Science and Technology of India; the BK21 program of the Ministry of Education of Korea, the CHEP SRC program and Basic Research program (grant No. R01-2005-000-10089-0) of the Korea Science and Engineering Foundation, and the Pure Basic Research Group program of the Korea Research Foundation; the Polish State Committee for Scientific Research; the Ministry of Science and Technology of the Russian Federation; the Slovenian Research Agency; the Swiss National Science Foundation; the National Science Council and the Ministry of Education of Taiwan; and the U.S. Department of Energy.

## APPENDIX A: PDFS FOR TIME-DEPENDENT DALITZ PLOT ANALYSIS

In this section, we describe the details of the PDF for each component, which appear in equations (31)-(34).

### 1. Signal PDF

#### a. PDF for correctly reconstructed events

In terms of the event fractions for the  $l^{\text{th}}$  flavor tagging region ( $\mathcal{F}_{\text{true}}^l$ ), the Dalitz plot dependent efficiency ( $\epsilon^l$ ), the  $\pi^0$  momentum dependent efficiency correction taking account of the difference between data and MC ( $\epsilon'$ ), wrong tag fraction ( $w_l$ ), and the wrong tag fraction difference between  $B^0$  and  $\bar{B}^0$  ( $\Delta w_l$ ), the PDF for correctly reconstructed events is given by

$$p_{\text{true}}^l(\Delta E, M_{\text{bc}}; m', \theta'; \Delta t, q_{\text{tag}}; p_{\pi^0}) = \mathcal{F}^l \cdot p_{\text{true}}(\Delta E, M_{\text{bc}}; p_{\pi^0}) \cdot \epsilon^l(m', \theta') \epsilon'(p_{\pi^0}) \cdot |\det \mathbf{J}(m', \theta')| \cdot p_{\text{true}}^l(m', \theta'; \Delta t, q_{\text{tag}}), \quad (\text{A1})$$

where

$$p_{\text{true}}^l(m', \theta'; \Delta t, q_{\text{tag}}) = \frac{e^{-|\Delta t|/\tau_{B^0}}}{4\tau_{B^0}} \cdot \left\{ (1 - q_{\text{tag}}\Delta w_l)(|A_{3\pi}|^2 + |\bar{A}_{3\pi}|^2) + q_{\text{tag}}(1 - 2w_l) \cdot \left[ -(|A_{3\pi}|^2 - |\bar{A}_{3\pi}|^2) \cos(\Delta m_d \Delta t) + 2\text{Im}[\frac{q}{p} \bar{A}_{3\pi} A_{3\pi}^*] \sin(\Delta m_d \Delta t) \right] \right\}. \quad (\text{A2})$$

For the  $\Delta t$  PDF, the above equation is convolved with the resolution function [14]. The  $\Delta E$ - $M_{\text{bc}}$  PDF is normalized such that

$$\iint_{\text{signal region}} d\Delta E \, dM_{\text{bc}} \, p_{\text{true}}(\Delta E, M_{\text{bc}}; p_{\pi^0}) = 1 \quad (\forall p_{\pi^0}), \quad (\text{A3})$$

since we define the Dalitz plot efficiency for events inside the signal region. With the PDFs in the  $\Delta t$ - $q_{\text{tag}}$  direction being also normalized to be unity, the integral inside the signal region,  $n_{\text{true}}$ , is,

$$n_{\text{true}} = \sum_l n_{\text{true}}^l, \quad (\text{A4})$$

$$n_{\text{true}}^l \equiv \sum_{q_{\text{tag}}} \int d\Delta t \iint_{\text{signal region}} d\Delta E \, dM_{\text{bc}} \iint_{\text{SDP, Veto}} dm' \, d\theta' \, p_{\text{true}}^l(\Delta E, M_{\text{bc}}; m', \theta'; \Delta t, q_{\text{tag}}; p_{\pi^0}) \quad (\text{A5})$$

$$= \mathcal{F}_{\text{true}}^l \iint_{\text{SDP, Veto}} dm' \, d\theta' \, \epsilon_{\text{true}}^l(m', \theta') \, \epsilon'(p_{\pi^0}) |\det \mathbf{J}| (|A_{3\pi}|^2 + |\bar{A}_{3\pi}|^2) , \quad (\text{A6})$$

where the correlation between  $p_{\pi^0}$  and  $m'$  is properly taken into account in the integration of the last line. The notation  $\iint_{\text{SDP, Veto}} dm' \, d\theta'$  means integration over the square Dalitz plot with the vetoed region in the Dalitz plot taken into account.

The  $\pi^0$  momentum dependent  $\Delta E$ - $M_{\text{bc}}$  PDF,  $p_{\text{true}}(\Delta E, M_{\text{bc}}; p_{\pi^0})$ , is modeled using MC-simulated events in a binned histogram interpolated in the  $p_{\pi^0}$  direction, to which a small correction obtained with  $\bar{B}^0 \rightarrow \rho^- D^{(*)+}$  is applied to account for the difference between MC and data.

The Dalitz plot distribution is smeared and distorted by detection efficiencies and detector resolutions. We obtain the signal Dalitz plot efficiency from MC to take the former into account. We introduce a dependence of the efficiency on the  $r$  region,  $\epsilon_{\text{true}}^l$ , since a significant dependence is observed in MC. Small corrections,  $\epsilon'(p_{\pi^0})$ , are also applied to the MC-determined efficiency to account for differences between MC and data. We use  $\bar{B}^0 \rightarrow \rho^- D^{(*)+}$ ,  $\bar{B}^0 \rightarrow \pi^- D^{*-}$ ,  $B^- \rightarrow \rho^- D^0$  and  $B^- \rightarrow \pi^- D^0$  decays to obtain the correction factors. The detector resolutions are small compared to the widths of  $\rho(770)$  resonances; this is confirmed by MC to be a negligibly small effect.

### b. PDF for SCF events

Approximately 20% of signal candidates are SCFs, which are subdivided into  $\sim 4\%$  of NR SCF and  $\sim 16\%$  of CR SCF. It is therefore important to develop a model that describes the SCF well. The time-dependent PDF for SCF events is defined as

$$p_i^l(\Delta E, M_{\text{bc}}; m', \theta'; \Delta t, q_{\text{tag}}) = \mathcal{F}_i^l \cdot p_i(\Delta E, M_{\text{bc}}; s_i) \cdot p_i(m', \theta'; \Delta t, q_{\text{tag}}) , \quad (i = \text{NR, CR}) \quad (\text{A7})$$

where  $\mathcal{F}_i^l$  is the event fraction in each tagging  $r$ -bin and

$$p_i(m', \theta'; \Delta t, q_{\text{tag}}) = \frac{e^{-|\Delta t|/\tau_i}}{4\tau_i} \cdot \left\{ (1 - q_{\text{tag}} \Delta w_l^i) p_i^{\text{Life}}(m', \theta') + q_{\text{tag}} (1 - 2w_l^i) \cdot [-p_i^{\text{Cos}}(m', \theta') \cos(\Delta m_d \Delta t) + p_i^{\text{Sin}}(m', \theta') \sin(\Delta m_d \Delta t)] \right\} . \quad (\text{A8})$$

The  $\Delta E$ - $M_{\text{bc}}$  PDF is normalized inside the signal region as

$$\iint_{\text{signal region}} d\Delta E \, dM_{\text{bc}} \, p_i(\Delta E, M_{\text{bc}}; s_i) = 1 \quad (\forall s_i) . \quad (\text{A9})$$

With the PDFs in the  $\Delta t$ - $q_{\text{tag}}$  direction being normalized to unity and  $\sum_l \mathcal{F}_i^l = 1$ , the integral inside the signal region,  $n_i$ , is

$$n_i \equiv \sum_l \sum_{q_{\text{tag}}} \int d\Delta t \iint_{\text{signal region}} d\Delta E \, dM_{\text{bc}} \iint_{\text{SDP, Veto}} dm' \, d\theta' \, p_i^l(\Delta E, M_{\text{bc}}; m', \theta'; \Delta t, q_{\text{tag}}) \quad (\text{A10})$$

$$= \iint_{\text{SDP, Veto}} dm' \, d\theta' \, p_i^{\text{Life}}(m', \theta') . \quad (\text{A11})$$

We find that the  $\Delta E$ - $M_{bc}$  distribution for SCF has a sizable correlation with Dalitz plot variables, but with only one of its two dimensions. We thus introduce a model with dependences on the Dalitz plot variable  $s_i$ . The variable  $s_{\text{CR}} = s_{\pm} \equiv \max(s_+, s_-)$  is used, because the CR SCF can be divided into a  $\pi^+$  replaced SCF and a  $\pi^-$  replaced SCF, where  $s_-$  ( $s_+$ ) is used for  $\pi^+$  ( $\pi^-$ ) replaced SCF. Here, we exploit the fact that almost all of the  $\pi^+$  ( $\pi^-$ ) replaced SCF distributes in the region of  $s_+ < s_-$  ( $s_+ > s_-$ ). For the NR SCF,  $s_{\text{NR}} = s_0$ . This parameterization models the correlation quite well, with each of the parameters  $s_i$  reasonably related to the kinematics of replaced tracks.

Since track ( $\pi$ ) replacement changes the measured kinematic variables, the SCF events “migrate” in the Dalitz plot from the correct (or generated) position to the observed position. Using MC, we determine resolution functions  $R_i(m'_{\text{obs}}, \theta'_{\text{obs}}; m'_{\text{gen}}, \theta'_{\text{gen}})$  to describe this “migration” effect, where  $(m'_{\text{obs}}, \theta'_{\text{obs}})$  and  $(m'_{\text{gen}}, \theta'_{\text{gen}})$  are the observed and the generated (correct) positions in the Dalitz plot, respectively. Together with the efficiency function  $\epsilon_i(m'_{\text{gen}}, \theta'_{\text{gen}})$ , which is also obtained with MC, the Dalitz plot PDF for SCF is described as

$$p_i^j(m', \theta') = [(R_i \cdot \epsilon_i) \otimes p_{\text{gen}}^j](m', \theta') \quad (\text{A12})$$

$$\equiv \iint_{\text{SDP}} dm'_{\text{gen}} d\theta'_{\text{gen}} R_i(m', \theta'; m'_{\text{gen}}, \theta'_{\text{gen}}) \cdot \epsilon_i(m'_{\text{gen}}, \theta'_{\text{gen}}) \cdot p_{\text{gen}}^j(m'_{\text{gen}}, \theta'_{\text{gen}}) \quad (\text{A13})$$

$$(i = \text{CR, NR}, \quad j = \text{Life, Cos, Sin})$$

where

$$p_{\text{gen}}^{\text{Life}}(m'_{\text{gen}}, \theta'_{\text{gen}}) = |\det \mathbf{J}|(|A_{3\pi}|^2 + |\overline{A}_{3\pi}|^2), \quad (\text{A14})$$

$$p_{\text{gen}}^{\text{Cos}}(m'_{\text{gen}}, \theta'_{\text{gen}}) = |\det \mathbf{J}|(|A_{3\pi}|^2 - |\overline{A}_{3\pi}|^2), \quad (\text{A15})$$

$$p_{\text{gen}}^{\text{Sin}}(m'_{\text{gen}}, \theta'_{\text{gen}}) = |\det \mathbf{J}| 2 \text{Im} \left[ \frac{q}{p} \overline{A}_{3\pi} A_{3\pi}^* \right]. \quad (\text{A16})$$

For the NR SCF, the shape of the  $\Delta t$  PDF defined in equation (A8) is exactly the same as correctly reconstructed signal, i.e.,  $\tau_{\text{NR}} = \tau_{B^0}$ ,  $w_l^{\text{NR}} = w_l$ , and  $\Delta w_l^{\text{NR}} = \Delta w_l$ , since the replaced track,  $\pi^0$ , is not used for either vertexing or flavor tagging. On the other hand, for the CR SCF, the  $\Delta t$  PDF is different from correctly reconstructed signal, since the replaced  $\pi^\pm$  is used for both vertexing and flavor tagging. Thus, we use MC-simulated CR SCF events to obtain  $\tau_{\text{CR}}$ ,  $w_l^{\text{CR}}$ , and  $\Delta w_l^{\text{CR}}$ , which are different from those of correctly reconstructed signal events. In particular,  $\Delta w_l^{\text{CR}}$  is opposite in sign for the  $\pi^+$  and  $\pi^-$  replaced SCFs, which is due to the fact that the replaced  $\pi^\pm$  tends to be directly used for flavor tagging in the slow pion category.

## 2. Continuum PDF

The PDF for the continuum background is

$$p_{qq}^l(\Delta E, M_{bc}; m', \theta'; \Delta t, q_{\text{tag}}) = \mathcal{F}_{qq}^l \cdot p_{qq}^l(\Delta E, M_{bc}) \cdot p_{qq}(m', \theta'; \Delta E, M_{bc}) \cdot \left[ \frac{1+q_{\text{tag}} A^l(m', \theta')}{2} \right] \cdot p_{qq}(\Delta t), \quad (\text{A17})$$

where  $\mathcal{F}_{qq}^l$  is the event fraction for each  $r$  region obtained in the signal yield fit. All the terms on the right hand side of the equation are normalized to be unity so that

$$\sum_l \sum_{q_{\text{tag}}} \int d\Delta t \iint_{\text{signal region}} d\Delta E \, dM_{\text{bc}} \iint_{\text{SDP, Veto}} dm' \, d\theta' \, p_{qq}^l(\Delta E, M_{\text{bc}}; m', \theta'; \Delta t, q_{\text{tag}}) = 1. \quad (\text{A18})$$

Since the allowed kinematic region is dependent on  $\Delta E$  and  $M_{\text{bc}}$ , the Dalitz plot distribution is dependent on  $\Delta E$  and  $M_{\text{bc}}$ . We define a  $\Delta E$ - $M_{\text{bc}}$  independent PDF,  $p_{qq}(m'_{\text{scale}}, \theta')$ , where  $m'_{\text{scale}}$  is a re-defined SDP variable with the kinematic effect taken into account as

$$m'_{\text{scale}} \equiv \frac{1}{\pi} \arccos \left( 2 \frac{m_0 - m_0^{\min}}{m_0^{\max} - m_0^{\min} + \Delta E + \Delta M_{\text{bc}}} - 1 \right), \quad (\text{A19})$$

where

$$\Delta M_{\text{bc}} \equiv M_{\text{bc}} - m_{B^0}. \quad (\text{A20})$$

Using the  $\Delta E$ - $M_{\text{bc}}$  independent PDF,  $p_{qq}(m', \theta'; \Delta E, M_{\text{bc}})$  is described as

$$p_{qq}(m', \theta'; \Delta E, M_{\text{bc}}) = \frac{1}{N(\Delta E + \Delta M_{\text{bc}})} \cdot \frac{\sin(\pi m')}{\sin(\pi m'_{\text{scale}})} \cdot p_{qq}(m'_{\text{scale}}, \theta') \quad (\text{A21})$$

for the region,  $m_0^{\min} < m_0 < \min(m_0^{\max}, m_0^{\max} + \Delta E + \Delta M_{\text{bc}})$  ( $p_{qq} = 0$  otherwise), where  $N(\Delta E + \Delta M_{\text{bc}})$  and  $\sin(\pi m')/\sin(\pi m'_{\text{scale}})$  are a normalization factor and the Jacobian for the parameter transformation of  $m'_{\text{scale}} \rightarrow m'$ , respectively. We obtain the  $p_{qq}(m'_{\text{scale}}, \theta')$  distribution from data in part of the sideband region,  $-0.1 \text{ GeV} < \Delta E < 0.2 \text{ GeV}$  and  $5.2 \text{ GeV}/c^2 < M_{\text{bc}} < 5.26 \text{ GeV}/c^2$ , where the contribution from  $B\bar{B}$  background is negligible.

Since we find significant flavor asymmetry depending on the location in the Dalitz plot, we introduce the following term to take account of it:

$$\frac{1 + q_{\text{tag}} A^l(m', \theta')}{2}, \quad (\text{A22})$$

which is  $r$  region dependent. The asymmetry is anti-symmetric in the direction of  $\theta'$ , i.e.,  $A^l(m', \theta') > 0$  ( $A^l(m', \theta') < 0$ ) in the region of  $\theta' > 0.5$  ( $\theta' < 0.5$ ), and the size of the asymmetry is  $\sim 20\%$  at most in the best  $r$  region. This effect is due to the jet-like topology of continuum events; when an event has a high momentum  $\pi^-$  ( $\pi^+$ ) on the  $CP$  side, the highest momentum  $\pi$  on the tag side tends to have  $+$  ( $-$ ) charge. The highest momentum  $\pi$  on the tag side with  $+$  ( $-$ ) charge tags the flavor as  $B^0$  ( $\bar{B}^0$ ). Since an event with a high momentum  $\pi^-$  ( $\pi^+$ ) resides in the region  $\theta' > 0.5$  ( $\theta' < 0.5$ ), a continuum event in the region  $\theta' > 0.5$  ( $\theta' < 0.5$ ) tends to be tagged as  $B^0$  ( $\bar{B}^0$ ). We again parameterize the  $A^l(m', \theta')$  in a  $\Delta E$ - $M_{\text{bc}}$  independent way as

$$A^l(m', \theta') = A^l(m'_{\text{scale}}, \theta'), \quad (\text{A23})$$

and model with a two-dimensional polynomial, whose coefficients are determined by a fit to data in the sideband region.

### 3. $B\bar{B}$ background PDF

The treatment of  $B\bar{B}$  background is different for  $CP$  eigenstate modes and flavor specific or charged modes. The PDF for the  $CP$  eigenstate modes is

$$p_{BB}^l(\Delta E, M_{bc}; m', \theta'; \Delta t, q_{tag}) = \mathcal{F}_{BB}^l \cdot p_{BB}(\Delta E, M_{bc}) \cdot p_{BB}(m', \theta') \cdot p_{BB}(\Delta t, q_{tag}), \quad (\text{A24})$$

where  $p_{BB}(\Delta t, q_{tag})$  is a time-dependent  $CP$  violation PDF normalized as

$$\sum_{q_{tag}} \int d\Delta t p_{BB}(\Delta t, q_{tag}) = 1. \quad (\text{A25})$$

For the flavor specific or charged modes, the PDF is

$$p_{BB}^l(\Delta E, M_{bc}; m', \theta'; \Delta t, q_{tag}) = \mathcal{F}_{BB}^l \cdot p_{BB}(\Delta E, M_{bc}) \sum_{q_{rec}} p_{BB}(m', \theta'; q_{rec}) \cdot p_{BB}(\Delta t, q_{tag}, q_{rec}), \quad (\text{A26})$$

where the Dalitz plot PDF  $p_{BB}(m', \theta'; q_{rec})$  is dependent on the true flavor of the  $CP$  (fully reconstructed) side,  $q_{rec}$ , and the time dependent part is a mixing PDF (lifetime PDF with flavor asymmetry) for flavor specific (charged) modes. The  $\Delta t$  PDF is normalized as

$$\sum_{q_{tag}} \sum_{q_{rec}} \int d\Delta t p_{BB}(\Delta t, q_{tag}, q_{rec}) = 1. \quad (\text{A27})$$

The  $\Delta E$ - $M_{bc}$  PDF and Dalitz plot PDF are obtained mode-by-mode from MC. The Dalitz plot PDF of the  $CP$  eigenstate modes is assumed to have following symmetry

$$p_{BB}(m', \theta') = p_{BB}(m', 1 - \theta'), \quad (\text{A28})$$

while that of flavor specific and charged modes is assumed to have following symmetry

$$p_{BB}(m', \theta'; q_{rec}) = p_{BB}(m', 1 - \theta'; -q_{rec}). \quad (\text{A29})$$

The total PDF of  $B\bar{B}$  background is a linear combination of each mode with efficiencies and branching fractions taken into account.

## APPENDIX B: CORRELATION MATRIX OF THE FIT RESULT

Tables VI-VIII show the correlation matrix for the 26 parameters determined in the time-dependent Dalitz plot analysis, corresponding to the total error matrix with statistical and systematic error matrices combined. We assume no correlation for the systematic errors.

TABLE VI: Correlation matrix (1) of the 26 fitted parameters, with statistical and systematic errors combined.

	$U_-^+$	$U_0^+$	$U_{+-}^{+, \text{Re}}$	$U_{+0}^{+, \text{Re}}$	$U_{-0}^{+, \text{Re}}$	$U_{+-}^{+, \text{Im}}$	$U_{+0}^{+, \text{Im}}$	$U_{-0}^{+, \text{Im}}$
$U_-^+$	+1.00							
$U_0^+$	+0.21	+1.00						
$U_{+-}^{+, \text{Re}}$	+0.05	+0.03	+1.00					
$U_{+0}^{+, \text{Re}}$	+0.09	+0.01	+0.01	+1.00				
$U_{-0}^{+, \text{Re}}$	-0.02	-0.09	+0.01	+0.01	+1.00			
$U_{+-}^{+, \text{Im}}$	+0.02	+0.01	+0.03	+0.00	-0.00	+1.00		
$U_{+0}^{+, \text{Im}}$	-0.04	-0.09	-0.00	+0.14	+0.02	-0.00	+1.00	
$U_{-0}^{+, \text{Im}}$	-0.13	-0.10	-0.01	-0.02	+0.02	-0.00	+0.02	+1.00
$U_+^-$	+0.05	+0.02	-0.00	-0.01	+0.00	-0.02	-0.01	-0.01
$U_-^-$	-0.22	-0.07	-0.03	-0.03	-0.03	-0.01	+0.01	+0.02
$U_0^-$	+0.05	+0.09	+0.01	+0.00	-0.04	+0.00	-0.05	-0.06
$U_{+-}^{-, \text{Re}}$	-0.04	-0.02	-0.06	-0.01	-0.00	+0.02	+0.00	+0.01
$U_{+0}^{-, \text{Re}}$	-0.05	-0.02	-0.00	-0.13	-0.00	+0.00	-0.04	+0.02
$U_{-0}^{-, \text{Re}}$	-0.02	-0.05	-0.00	-0.00	+0.08	-0.00	+0.02	+0.07
$U_{+-}^{-, \text{Im}}$	-0.04	-0.02	-0.00	-0.01	-0.00	+0.05	+0.00	+0.01
$U_{+0}^{-, \text{Im}}$	-0.04	-0.08	-0.01	-0.06	+0.01	-0.00	-0.08	+0.02
$U_{-0}^{-, \text{Im}}$	-0.02	-0.02	-0.00	-0.00	-0.03	-0.00	+0.00	-0.12
$I_+$	+0.00	+0.00	-0.01	-0.01	-0.00	-0.02	-0.02	-0.00
$I_-$	+0.07	+0.03	-0.01	+0.01	-0.01	+0.03	-0.00	+0.01
$I_0$	+0.01	+0.01	+0.00	+0.01	+0.01	+0.00	-0.02	-0.03
$I_{+-}^{\text{Re}}$	-0.02	-0.00	+0.01	+0.00	+0.00	-0.20	+0.00	+0.00
$I_{+0}^{\text{Re}}$	+0.00	+0.02	+0.00	-0.12	-0.01	+0.00	-0.01	+0.00
$I_{-0}^{\text{Re}}$	-0.04	+0.02	-0.01	-0.01	-0.11	+0.00	-0.01	-0.25
$I_{+-}^{\text{Im}}$	-0.02	-0.01	+0.09	-0.00	-0.00	+0.03	+0.00	+0.00
$I_{+0}^{\text{Im}}$	+0.01	-0.02	+0.00	+0.04	+0.00	+0.00	+0.07	+0.00
$I_{-0}^{\text{Im}}$	-0.07	-0.04	-0.01	-0.01	-0.09	-0.01	+0.01	+0.08

TABLE VII: Correlation matrix (2) of the 26 fitted parameters, with statistical and systematic errors combined.

	$U_+^-$	$U_-^-$	$U_0^-$	$U_{+-}^{-,\text{Re}}$	$U_{+0}^{-,\text{Re}}$	$U_{-0}^{-,\text{Re}}$	$U_{+-}^{-,\text{Im}}$	$U_{+0}^{-,\text{Im}}$	$U_{-0}^{-,\text{Im}}$
$U_+^-$	+1.00								
$U_-^-$	-0.06	+1.00							
$U_0^-$	+0.00	-0.00	+1.00						
$U_{+-}^{-,\text{Re}}$	-0.04	+0.02	-0.00	+1.00					
$U_{+0}^{-,\text{Re}}$	-0.17	+0.03	-0.08	+0.01	+1.00				
$U_{-0}^{-,\text{Re}}$	+0.01	-0.10	-0.18	-0.00	+0.02	+1.00			
$U_{+-}^{-,\text{Im}}$	+0.06	-0.00	-0.00	+0.16	-0.01	+0.00	+1.00		
$U_{+0}^{-,\text{Im}}$	-0.00	+0.01	-0.08	+0.00	+0.03	+0.02	+0.00	+1.00	
$U_{-0}^{-,\text{Im}}$	-0.00	+0.02	+0.01	-0.00	-0.00	+0.02	+0.00	+0.00	+1.00
$I_+$	-0.02	-0.00	-0.00	+0.02	+0.00	+0.00	-0.02	+0.01	+0.01
$I_-$	-0.00	-0.02	+0.01	+0.02	-0.00	-0.04	-0.01	-0.01	-0.08
$I_0$	-0.00	-0.01	+0.07	+0.00	+0.01	+0.02	-0.00	-0.04	-0.04
$I_{+-}^{\text{Re}}$	+0.02	+0.01	-0.00	-0.04	-0.00	-0.00	-0.19	-0.00	+0.00
$I_{+0}^{\text{Re}}$	-0.00	+0.00	+0.01	-0.00	+0.06	-0.01	+0.00	+0.11	+0.01
$I_{-0}^{\text{Re}}$	-0.01	+0.07	+0.05	+0.01	-0.00	-0.09	+0.00	-0.01	+0.13
$I_{+-}^{\text{Im}}$	+0.01	+0.03	-0.00	+0.06	-0.00	-0.00	+0.05	+0.00	+0.00
$I_{+0}^{\text{Im}}$	+0.02	-0.00	-0.01	-0.00	-0.25	-0.00	+0.00	-0.02	+0.01
$I_{-0}^{\text{Im}}$	-0.00	+0.03	-0.01	+0.00	+0.00	+0.15	+0.01	+0.02	+0.10

TABLE VIII: Correlation matrix (3) of the 26 fitted parameters, with statistical and systematic errors combined.

	$I_+$	$I_-$	$I_0$	$I_{+-}^{\text{Re}}$	$I_{+0}^{\text{Re}}$	$I_{-0}^{\text{Re}}$	$I_{+-}^{\text{Im}}$	$I_{+0}^{\text{Im}}$	$I_{-0}^{\text{Im}}$
$I_+$	+1.00								
$I_-$	-0.06	+1.00							
$I_0$	+0.01	+0.02	+1.00						
$I_{+-}^{\text{Re}}$	-0.08	-0.00	-0.00	+1.00					
$I_{+0}^{\text{Re}}$	-0.02	-0.00	-0.10	+0.00	+1.00				
$I_{-0}^{\text{Re}}$	-0.01	+0.14	+0.00	+0.00	+0.00	+1.00			
$I_{+-}^{\text{Im}}$	-0.03	-0.02	-0.00	-0.28	+0.00	+0.00	+1.00		
$I_{+0}^{\text{Im}}$	-0.13	+0.01	-0.12	+0.01	-0.11	-0.00	+0.01	+1.00	
$I_{-0}^{\text{Im}}$	+0.01	-0.12	-0.19	+0.00	+0.03	+0.03	+0.00	+0.03	+1.00

## APPENDIX C: METHOD OF $\phi_2$ CONSTRAINT

### 1. Formalism

We define amplitudes as

$$A^+ \equiv A(B^0 \rightarrow \rho^+ \pi^-) , \quad (C1)$$

$$A^- \equiv A(B^0 \rightarrow \rho^- \pi^+) , \quad (C2)$$

$$A^0 \equiv A(B^0 \rightarrow \rho^0 \pi^0) , \quad (C3)$$

$$A^{+0} \equiv A(B^+ \rightarrow \rho^+ \pi^0) , \quad (C4)$$

$$A^{0+} \equiv A(B^+ \rightarrow \rho^0 \pi^+) , \quad (C5)$$

and

$$\bar{A}^+ \equiv \frac{p}{q} A(\bar{B}^0 \rightarrow \rho^+ \pi^-) , \quad (C6)$$

$$\bar{A}^- \equiv \frac{p}{q} A(\bar{B}^0 \rightarrow \rho^- \pi^+) , \quad (C7)$$

$$\bar{A}^0 \equiv \frac{p}{q} A(\bar{B}^0 \rightarrow \rho^0 \pi^0) , \quad (C8)$$

$$A^{-0} \equiv \frac{p}{q} A(B^- \rightarrow \rho^- \pi^0) , \quad (C9)$$

$$A^{0-} \equiv \frac{p}{q} A(B^- \rightarrow \rho^0 \pi^-) . \quad (C10)$$

These amplitudes are obtained from 1) 26 measurements determined in the time-dependent Dalitz plot analysis as well as 2) branching fractions and asymmetry measurements, and give a constraint on  $\phi_2$ .

Equations (21)-(25) define the relations between the amplitudes for the neutral modes and the parameters determined in the time-dependent Dalitz plot analysis. The relations between the branching fractions and asymmetries, and the amplitudes are

$$\mathcal{B}(\rho^\pm \pi^\mp) = c \cdot (|A^+|^2 + |A^-|^2 + |\bar{A}^+|^2 + |\bar{A}^-|^2) \cdot \tau_{B^0} , \quad (C11)$$

$$\mathcal{B}(\rho^+ \pi^0) = c \cdot (|A^{+0}|^2 + |A^{-0}|^2) \cdot \tau_{B^+} , \quad (C12)$$

$$\mathcal{B}(\rho^0 \pi^+) = c \cdot (|A^{0+}|^2 + |A^{0-}|^2) \cdot \tau_{B^+} , \quad (C13)$$

$$\mathcal{A}(\rho^+ \pi^0) = \frac{|A^{-0}|^2 - |A^{+0}|^2}{|A^{-0}|^2 + |A^{+0}|^2} , \quad (C14)$$

$$\mathcal{A}(\rho^0 \pi^+) = \frac{|A^{0-}|^2 - |A^{0+}|^2}{|A^{0-}|^2 + |A^{0+}|^2} , \quad (C15)$$

where  $c$  is a constant and the lifetimes  $\tau_{B^0}$  and  $\tau_{B^+}$  are introduced to take account of the total width difference between  $B^0$  and  $B^+$ . Note that we do not use quasi-two-body parameters

related to neutral modes except for  $\mathcal{B}(\rho^\pm\pi^\mp)$ , since they are included in the Dalitz plot parameters.

The amplitudes are expected to follow  $SU(2)$  isospin symmetry to a good approximation [7, 8]

$$\begin{aligned} A^+ + A^- + 2A^0 &= \tilde{A}^+ + \tilde{A}^- + 2\tilde{A}^0 \\ &= \sqrt{2}(A^{+0} + A^{0+}) = \sqrt{2}(\tilde{A}^{-0} + \tilde{A}^{0-}), \end{aligned} \quad (\text{C16})$$

$$A^{+0} - A^{0+} - \sqrt{2}(A^+ - A^-) = \tilde{A}^{-0} - \tilde{A}^{0-} - \sqrt{2}(\tilde{A}^- - \tilde{A}^+), \quad (\text{C17})$$

where

$$\tilde{A}^\kappa \equiv e^{-2i\phi_2} \bar{A}^\kappa, \quad \tilde{A}^{-0} \equiv e^{-2i\phi_2} A^{-0}, \quad \text{and} \quad \tilde{A}^{0-} \equiv e^{-2i\phi_2} A^{0-}. \quad (\text{C18})$$

Note that there is an inconsistency in equation (C17) between Ref. [7] and Ref. [8]; we follow the treatment of Ref. [7], which we believe is correct.

## 2. Parameterization

Here we give two examples of the parameterization of the amplitudes. The first example may be more intuitive, while the second example is well behaved in the fit. The results are independent of the parameterizations with respect to the constraint on  $\phi_2$ .

### a. Amplitude parameterization

We can parameterize the amplitudes as follows [7]

$$A^+ = e^{-i\phi_2} T^+ + P^+, \quad (\text{C19})$$

$$A^- = e^{-i\phi_2} T^- + P^-, \quad (\text{C20})$$

$$A^0 = e^{-i\phi_2} T^0 - \frac{1}{2}(P^+ + P^-), \quad (\text{C21})$$

$$\sqrt{2}A^{+0} = e^{-i\phi_2} T^{+0} + P^+ - P^-, \quad (\text{C22})$$

$$\sqrt{2}A^{0+} = e^{-i\phi_2} (T^+ + T^- + 2T^0 - T^{+0}) - P^+ + P^-, \quad (\text{C23})$$

and

$$\bar{A}^+ = e^{+i\phi_2} T^- + P^-, \quad (\text{C24})$$

$$\bar{A}^- = e^{+i\phi_2} T^+ + P^+, \quad (\text{C25})$$

$$\bar{A}^0 = e^{+i\phi_2} T^0 - \frac{1}{2}(P^+ + P^-), \quad (\text{C26})$$

$$\sqrt{2}\bar{A}^{-0} = e^{+i\phi_2} T^{+0} + P^+ - P^-, \quad (\text{C27})$$

$$\sqrt{2}\bar{A}^{0-} = e^{+i\phi_2} (T^+ + T^- + 2T^0 - T^{+0}) - P^+ + P^-, \quad (\text{C28})$$

where the overall phase is fixed with the convention  $\text{Im}T^+ = 0$ . Thus, there are 6 complex amplitudes,  $T^+, T^-, T^0, P^+, P^-,$  and  $T^{+0}$ , corresponding to 11 degrees of freedom; and  $\phi_2$ , corresponding to 12 degrees of freedom in total. This parameterization automatically satisfies the isospin relations without losing generality, i.e., the isospin relations are the only assumption here.

b. *Geometric parameterization*

We can parameterize the amplitudes using the geometric arrangement of Fig. 13 that satisfies the isospin relation of equation (C16). This figure is equivalent to Fig. 3 of Ref. [8], except that the sides corresponding to  $B^0 \rightarrow \rho^- \pi^+$  and  $B^0 \rightarrow \rho^0 \pi^0$  are swapped. This difference is not physically significant. We apply this modification only to obtain a better behaved parameterization; the parameterization here uses the angles  $\omega_-$  and  $\theta_-$  related to the process  $B^0(\bar{B}^0) \rightarrow \rho^- \pi^+$ , which are better behaved than those related to  $B^0(\bar{B}^0) \rightarrow \rho^0 \pi^0$ .

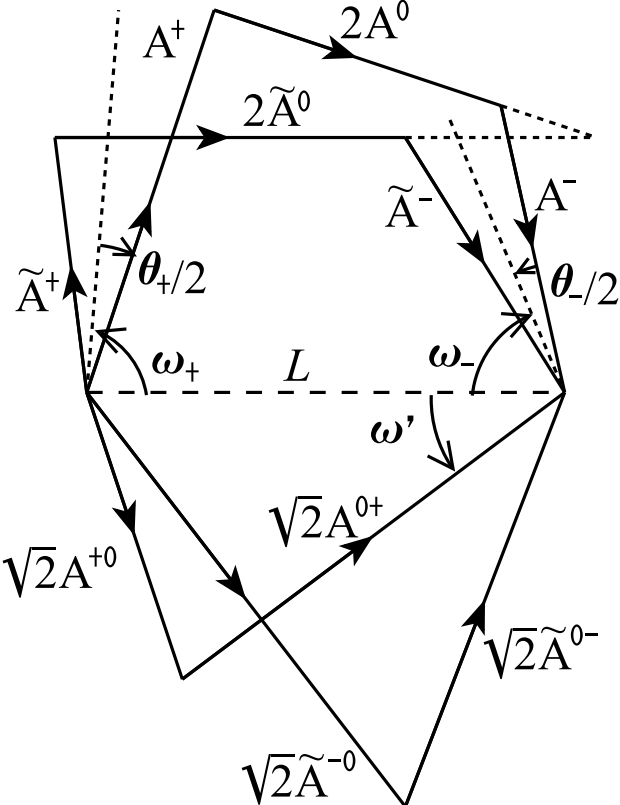


FIG. 13: Complex pentagons formed from the  $B \rightarrow \rho\pi$  decay amplitudes.

To parameterize the amplitudes, we use  $\phi_2$  and the following 11 geometric parameters:

$$\omega_+, \omega_-, \omega', \theta_+, \theta_-, b_+, b_-, b', a_+, a_-, L, \quad (C29)$$

where  $b$  and  $a$  *imply* branching fraction and asymmetry, respectively. In terms of these

parameters, the amplitudes can be described as follows

$$A^+ = e^{i(\omega_+ + \theta_+/2)} \sqrt{b_+(1 - a_+)/2}, \quad (\text{C30})$$

$$\tilde{A}^+ = e^{i(\omega_+ - \theta_+/2)} \sqrt{b_+(1 + a_+)/2}, \quad (\text{C31})$$

$$A^- = e^{i(\omega_- + \theta_-/2)} \sqrt{b_-(1 - a_-)/2}, \quad (\text{C32})$$

$$\tilde{A}^- = e^{i(\omega_- - \theta_-/2)} \sqrt{b_-(1 + a_-)/2}, \quad (\text{C33})$$

$$A^0 = (L - A^+ - A^-)/2, \quad (\text{C34})$$

$$\tilde{A}^0 = (L - \tilde{A}^+ - \tilde{A}^-)/2, \quad (\text{C35})$$

$$A^{0+} = e^{i\omega'} \sqrt{b'/2}, \quad (\text{C36})$$

$$A^{+0} = \frac{L}{\sqrt{2}} - A^{0+}, \quad (\text{C37})$$

$$\tilde{A}^{0-} = \frac{L}{2\sqrt{2}} - \left[ A^{+0} - A^{0+} - \sqrt{2}(A^+ - A^-) + \sqrt{2}(\tilde{A}^- - \tilde{A}^+) \right] / 2, \quad (\text{C38})$$

$$\tilde{A}^{-0} = \frac{L}{\sqrt{2}} - \tilde{A}^{0+}. \quad (\text{C39})$$

Equation (C38) exploits the isospin relation of equation (C17), which Fig. 13 does not incorporate geometrically. The phase  $\phi_2$  enters when the  $\tilde{A}$ 's are converted into  $\overline{A}$ 's with equation (C18). When we perform the analysis only with the time-dependent Dalitz plot observables and without the information from charged decay modes, we remove the parameters  $\omega'$  and  $b'$  from the fit and fix  $L$  to be a constant.

This geometric parameterization has a substantial advantage in terms of required computational resources, compared to the parameterization based on the  $T$  and  $P$  amplitudes described in the previous section. In the procedure to constrain  $\phi_2$ , the minimum  $\chi^2$  has to be calculated for each value of  $\phi_2$ . To avoid local minima, initial values of the parameters for the minimization have to be scanned and this inflates the computing time, which increases exponentially with the number of parameters. However, the number of parameters to be scanned decreases in the geometric parameterization. Among 11 parameters except for  $\phi_2$ , five of them,  $b_+, b_-, b', a_+$ , and  $a_-$ , are related to the branching fractions and asymmetries. Since in most cases they do not have multiple solutions, we do not have to scan the initial values of them. In addition, the optimum initial value for  $L$  can also be determined using other parameters and  $b_0$ , the nominal branching fraction of  $B^0 \rightarrow \rho^0 \pi^0$ , from the following relation

$$b_0 = \left| L - e^{i\omega_+} \sqrt{b_+/2} - e^{i\omega_-} \sqrt{b_-/2} \right|^2, \quad (\text{C40})$$

up to a two-fold ambiguity. Here  $b_0$  is calculated using the input parameters as

$$b_0 = \frac{U_0^+}{U_+^+ + U_-^+} \cdot \frac{\mathcal{B}(\rho^\pm \pi^\mp)}{c \cdot \tau_{B^0}}, \quad (\text{C41})$$

based on equations (21) and (C11). The explicit solution for the optimal initial value of  $L$  is

$$L = \text{Re}\gamma \pm \sqrt{b_0 - (\text{Im}\gamma)^2} \quad \left( \quad \gamma \equiv e^{i\omega_+} \sqrt{b_+/2} + e^{i\omega_-} \sqrt{b_-/2} \quad \right). \quad (\text{C42})$$

When  $b_0 - (\text{Im}\gamma)^2 < 0$ , there is no real-valued solution and  $L = \text{Re}\gamma$  is the optimum initial value. With the optimum values calculated above, the initial value of  $L$  does not have to be scanned, except for the two fold ambiguity. Consequently, the number of parameters to be scanned in this parameterization is only five, corresponding to  $\omega_+, \omega_-, \omega', \theta_+$ , and  $\theta_-$ , while all of 11 or maybe 10 parameters have to be scanned in the  $T$  and  $P$  amplitude parameterization. This leads to a substantial reduction of the computational resources required.

---

- [1] M. Kobayashi and T. Maskawa, *Prog. Theor. Phys.* **49**, 652 (1973).
- [2] A. B. Carter and A. I. Sanda, *Phys. Rev. Lett.* **45**, 952 (1980).
- [3] A. B. Carter and A. I. Sanda, *Phys. Rev.* **D23**, 1567 (1981).
- [4] I. I. Y. Bigi and A. I. Sanda, *Nucl. Phys.* **B193**, 85 (1981).
- [5] Throughout this paper, the inclusion of the charge conjugate decay mode is implied unless otherwise stated.
- [6] A. E. Snyder and H. R. Quinn, *Phys. Rev.* **D48**, 2139 (1993).
- [7] H. J. Lipkin, Y. Nir, H. R. Quinn, and A. Snyder, *Phys. Rev.* **D44**, 1454 (1991).
- [8] M. Gronau, *Phys. Lett.* **B265**, 389 (1991).
- [9] S. Kurokawa and E. Kikutani, *Nucl. Instrum. Meth.* **A499**, 1 (2003), and other papers included in this volume.
- [10] A. Abashian et al. (Belle Collaboration), *Nucl. Instrum. Meth.* **A479**, 117 (2002).
- [11] Y. Ushiroda (Belle SVD2 Group), *Nucl. Instrum. Meth.* **A511**, 6 (2003).
- [12] G. J. Gounaris and J. J. Sakurai, *Phys. Rev. Lett.* **21**, 244 (1968).
- [13] B. Aubert et al. (BaBar Collaboration) (2004), [hep-ex/0408099](#).
- [14] H. Tajima et al., *Nucl. Instrum. Meth.* **A533**, 370 (2004), [[hep-ex/0301026](#)].
- [15] H. Kakuno et al., *Nucl. Instrum. Meth.* **A533**, 516 (2004), [[hep-ex/0403022](#)].
- [16] K. Abe et al. (Belle Collaboration), *Phys. Rev.* **D71**, 072003 (2005), [[hep-ex/0408111](#)].
- [17] K. F. Chen et al. (Belle Collaboration), *Phys. Rev.* **D72**, 012004 (2005), [[hep-ex/0504023](#)].
- [18] H. Albrecht et al. (ARGUS Collaboration), *Phys. Lett.* **B241**, 278 (1990).
- [19] S. Eidelman et al. (Particle Data Group), *Phys. Lett.* **B592**, 1 (2004), and 2005 partial update (<http://pdg.lbl.gov>).
- [20] Heavy Flavor Averaging Group (HFAG) (2006), [hep-ex/0603003](#); and online update of Winter 2006 (<http://www.slac.stanford.edu/xorg/hfag>).
- [21] M. Ablikim et al. (BES Collaboration), *Phys. Lett.* **B598**, 149 (2004), [[hep-ex/0406038](#)].
- [22] H. Muramatsu et al. (CLEO Collaboration), *Phys. Rev. Lett.* **89**, 251802 (2002), [[hep-ex/0207067](#)].
- [23] E. M. Aitala et al. (E791 Collaboration), *Phys. Rev. Lett.* **86**, 770 (2001), [[hep-ex/0007028](#)].
- [24] O. Long, M. Baak, R. N. Cahn, and D. Kirkby, *Phys. Rev.* **D68**, 034010 (2003), [[hep-ex/0303030](#)].
- [25] J. Dragic et al. (Belle Collaboration), *Phys. Rev.* **D73**, 111105 (2006).
- [26] J. Charles et al. (CKMfitter Group), *Eur. Phys. J.* **C41**, 1 (2005), [[hep-ph/0406184](#)].
- [27] Strictly speaking, the difference between the  $\pi^\pm$  and  $\pi^0$  masses is taken into account and thus  $F_\pi(s_\pm)$  and  $F_\pi(s_0)$  are slightly different. The essential point here is, however, that one unique set of  $(\beta, \gamma)$  is used for all six  $(\overline{f}_\kappa)$ .
- [28]  $\Delta\chi^2(\phi_2)$  is usually expected to follow a  $\chi^2$  distribution with one degree of freedom and thus

the cumulative  $\chi^2$  distribution for one degree of freedom is usually used to convert  $\Delta\chi^2(\phi_2)$  into a  $1 - \text{C.L.}$  plot. A toy MC study shows, however, that this is not the case for  $B \rightarrow \rho\pi$ , and an analysis with this assumption yields confidence intervals with undercoverage. Thus, we perform a dedicated Toy MC study to obtain the confidence interval.